Domain Wall Characterization in Sub-μm Period Ferroelectric Crystals by Čerenkov Second Harmonic Generation

CHANG LIU

Master's Thesis at Kungliga Tekniska Högskolan
Supervisor: Carlota Canalias
Examiner: Valdas Pasiskevicius

TRITA-FYS 2015:04 ISSN 0280-316X ISRN KTH/FYS/–15:04—SE

"In all these cases the first step towards answering a question rationally is to understand it , which entails understanding the words in which it is posed. The reward for learning about their meanings or uses is that we are at the same time learning something of the canons for thinking logically about questions containing them. For they, like all other words, owe their meanings partly or wholly to their logical properties."

- Richard M. Hare, *Moral Thinking*, 1981

"We are at the very beginning of time for the human race. It is not unreasonable that we grapple with problems. But there are tens of thousands of years in the future. Our responsibility is to do what we can, learn what we can, improve the solutions, and pass them on. It is our responsibility to leave the people of the future a free hand. In the impetuous youth of humanity, we can make grave errors that can stunt our growth for a long time. This we will do if we say we have the answers now, so young and ignorant as we are. If we suppress all discussion, all criticism, proclaiming 'This is the answer, my friends; man is saved!' we will doom humanity for a long time to the chains of authority, confined to the limits of our present imagination. It has been done so many times before.

It is our responsibility as scientists, knowing the great progress which comes from a satisfactory philosophy of ignorance, the great progress which is the fruit of freedom of thought, to proclaim the value of this freedom; to teach how doubt is not to be feared but welcomed and discussed; and to demand this freedom as our duty to all coming generations."

- Richard P. Feynman, *The Value of Science*, 1988

Contents

Abstract

In this thesis, I proposed a new method to utilize Čerenkov Second Harmonic Generation (CSHG) for domain structure characterization, which is noninvasive and can probe deep in the crystal bulk. Based on Boyd and Kleinman's theory, I derived the coupled wave equations and the solution for CSHG with Gaussian laser beams in periodically poled crystals, according to which the CSHG power is proportional to the domain wall density (twice the reciprocal of the QPM grating period). Additionally, I explained the characteristic angle of nonlinear Čerenkov radiation with Fermat's principle.

In my experiments, the fundamental pump beam was launched along the $y-$axis of the QPM crystals and both branches of CSHG were detected: one with a CCD camera and the other one with a sensitive power meter. (R)KTP crystals with four different QPM grating periods were used for acquiring the calibration curve of CSHG power dependence upon the mean domain wall density. Afterwards, I measured the CSHG power from two sub-μm period crystals, where the regions close to the crystal surface were measured in order to use the etching pattern as a reference. By converting the CSHG power into the QPM grating period, the period distributions in these two crystals were evaluated. Compared to the known results from the etching patterns on the crystals, revealed by SEM photographs, these results were in good agreement. Finally, the measurement error in this method was proven to decrease with the QPM grating period so the results were more accurate for high domain wall densities.

Furthermore, by combining the calibration curve and the CSHG theory, the approximate value of the second-order nonlinear coefficient was evaluated and was found to be tens of times the bulk value. Thus the proposition of the existence of the enhanced nonlinearity at ferroelectric domain walls was verified.

Chapter 1

Introduction

Ever since the invention of laser, the study of optics at high intensities has opened a new gate in science: nonlinear optics. The demonstration of the optical second harmonic generation was published by Franken *et al.* [1], after which many important nonlinear optical phenomena were discovered, for example, the optical parametric oscillation, the self-focusing in a homogeneous liquid, optical solitons and supercontinuum. As a result, many applications were invented, such as Raman spectroscopy, THz generation, second harmonic generation microscopy and optical parametric oscillators. The field of nonlinear optics has been prospering for decades since then.

In nonlinear optical materials, the dispersion phenomenon gives rise to a phase mismatch between different frequencies, causing the generated wave field to evolve in a sinusoidal manner spatially. That leads to a very low conversion efficiency for nonlinear processes. To improve the efficiency, different techniques were proposed. Among these, quasi-phase-matching (QPM) is becoming more and more popular because of the great flexibility and extensive compatibility for different wavelengths and materials. Usually, QPM is achieved by electric field periodic poling. The idea is to flip the nonlinearity periodically where the generated wave field starts to decrease, so that the output power could increase monotonically, instead of oscillating sinusoidally. Thus, the conversion efficiency limit due to dispersion is then removed. Ferroelectric crystals are often used in this case, such as lithium niobate (LN), lithium tantalate (LT), potassium titanyl arsenate (KTA) and potassium titanyl phosphate (KTP).

Thus there is a need for a method to investigate the electric field poling quality of the QPM crystals for monitoring and controlling the grating structure. Currently, the investigation methods are mostly limited to the surface or thin films, such as scanning electron microscopy, atomic force microscopy and piezoelectric force microscopy. Selective etching is also frequently used, but it is both destructive and limited to the surface. The electro-optic effect and forward second harmonic generation are also used for real time poling control but one can only evaluate the

average domain situation over all domains, meaning these methods are not sensitive enough. Additionally, the current theories on CSHG of Gaussian beams are still not completely clear.

In this thesis, I proposed a theory for CSHG with Gaussian beams, including the coupled wave equations and the linear relation between the CSHG power and the domain wall density. Thus, a new method was then established to characterize the domain structure of sub-μm period ferroelectric materials. First, I measured the CSHG power as a linear function of the domain wall density with four reference crystals whose domain periods are already known; after that, I used this function as the calibration curve to convert the CSHG power from two different sub-μm period crystals to domain wall density. Since domain walls are the boundaries of domains, the domain characterization was then achieved.

Chapter 2

Basics of Nonlinear Optics

2.1 Introduction

According to basic electrodynamics, in the frequency domain, the electric polarization density $\mathscr{P}$ can be expressed in terms of the external field $\mathbf{E}$

$$\mathscr{P} = \varepsilon_0(\chi^{(1)}\mathbf{E} + \chi^{(2)}\mathbf{E}^2 + \chi^{(3)}\mathbf{E}^3 + \cdots) \tag{2.1}$$

in which $\chi^{(1)}$ is the first-order or linear susceptibility of the material, and $\chi^{(2)}$ and $\chi^{(3)}$ are the 2nd- and 3rd- order susceptibilities, respectively. When the field intensity is low, only the linear term is pronounced - just as in transmission, reflection and refraction. However, when the field intensity is high enough, the higher order terms will be significant. The electromagnetic waves start to interact with each other and the dielectric medium in a nonlinear fashion, which is the realm of nonlinear optics.

There are several nonlinear optical processes. In this thesis, second harmonic generation and sum frequency mixing are used. In a nonlinear optical process, if the pump photon energies are $\hbar\omega_1$ and $\hbar\omega_2$, the generated photon energy is $\hbar\omega_3$, and

$$\omega_3 = \omega_1 + \omega_2$$

it is called sum frequency mixing. Furthermore, if

$$\omega_1 = \omega_2$$

, it is defined as second harmonic generation.

2.2 The Nonlinearity Tensor

Due to the vector nature of fields, $\chi^{(1)}$ is a second-rank tensor, and $\chi^{(2)}$ and $\chi^{(3)}$ are third- and fourth- rank tensors, respectively. For second-order nonlinear processes

(nonresonant), the nonlinear polarization is [2]

$$(\mathscr{P}^{(2)}_{\omega_3})_\mu = \varepsilon_0 \sum_{\alpha_1\alpha_2} \sum_{\omega} K(-\omega_3;\omega_1,\omega_2)\chi^{(2)}_{\mu\alpha_1\alpha_2}(-\omega_3;\omega_1,\omega_2)(E_{\omega_1})_{\alpha_1}(E_{\omega_2})_{\alpha_2} \quad (2.2)$$

where

$$K(-\omega_3;\omega_1,\omega_2) = 2^{l+m-2}p \quad (2.3)$$

in which ω_i $(i = 1, 2, 3)$ are the wave frequencies, $l = 0$ if $\omega_3 = 0$ and $l = 1$ otherwise; m is the number of DC fundamental fields (i.e. ω_1,ω_2); $p = 1$ for $\omega_1 = \omega_2$ and $p = 2$ otherwise. The parameter $K(-\omega_3;\omega_1,\omega_2)$ takes care of the permutation symmetry, which is valid under the approximation of a lossless medium and nonresonant frequencies. Experimentalists prefer using the nonlinear d-tensor, which is half of the nonlinearity coefficient $\chi^{(2)}$.

$$(\mathscr{P}_\mu)_{\omega_3} = 2\varepsilon_0 K(-\omega_3;\omega_1,\omega_2)d_{\mu\alpha\beta}(-\omega_3;\omega_1,\omega_2)(E_\alpha)_{\omega_1}(E_\beta)_{\omega_2} \quad (2.4)$$

where α and β stand for the coordinate components x, y, and z. The fields $(E_\alpha)_{\omega_1}$ and $(E_\beta)_{\omega_2}$ can be swapped

$$d_{\mu\alpha\beta} = d_{\mu\beta\alpha} = d_{\mu m} \quad (2.5)$$

As a result, there are only 18 independent values in the 27-element d-tensor at most

$$d_{\mu xx} = d_{\mu 1},\ d_{\mu yy} = d_{\mu 2},\ d_{\mu zz} = d_{\mu 3},\ d_{\mu yz} = d_{\mu 4},\ d_{\mu xz} = d_{\mu 5},\ d_{\mu xy} = d_{\mu 6}$$

Thus, the relationship between the interacting electric fields and the second-order nonlinear polarization can be expressed as below [3]

$$\begin{bmatrix} (\mathscr{P}_x)^{(2)}_{\omega_3} \\ (\mathscr{P}_y)^{(2)}_{\omega_3} \\ (\mathscr{P}_z)^{(2)}_{\omega_3} \end{bmatrix} = 2\varepsilon_0 K(-\omega_3;\omega_1,\omega_2) \begin{bmatrix} d_{11}\cdots d_{16} \\ d_{21}\cdots d_{26} \\ d_{31}\cdots d_{36} \end{bmatrix} \begin{bmatrix} (E_x)_{\omega_1}(E_x)_{\omega_2} \\ (E_y)_{\omega_1}(E_y)_{\omega_2} \\ (E_z)_{\omega_1}(E_z)_{\omega_2} \\ (E_y)_{\omega_1}(E_z)_{\omega_2} + (E_z)_{\omega_1}(E_y)_{\omega_2} \\ (E_x)_{\omega_1}(E_z)_{\omega_2} + (E_z)_{\omega_1}(E_x)_{\omega_2} \\ (E_y)_{\omega_1}(E_x)_{\omega_2} + (E_x)_{\omega_1}(E_y)_{\omega_2} \end{bmatrix} \quad (2.6)$$

The second-order nonlinearity arises from the structural noncentrosymmetry. There are five common second order nonlinear processes: second harmonic generation (SHG), sum frequency mixing (SFM), optical rectification (EOR), difference frequency generation (DFG) and electrooptic modulation (EMO).

2.3 The Nonlinear Wave Equation

Based on Maxwell equations, we have a nonlinear wave equation in nonlinear optics

$$\nabla^2\mathbf{E} - \mu_0\varepsilon_0(1+\chi^{(1)}))\frac{\partial^2\mathbf{E}}{\partial t^2} = \mu_0\frac{\partial^2\mathscr{P}^{NL}}{\partial t^2} \tag{2.7}$$

The term with the nonlinear polarization $\mathscr{P}^{NL}$ is considered as a perturbation to the plane wave model. So for monochromatic waves propagating along z-axis, the real electric field can be expressed as (c.c. is short for complex conjugate here)

$$\mathbf{E}(t,z) = \frac{1}{2}[\mathbf{E}_\omega(z)\exp(i(\omega t - kz)) + c.c.] \tag{2.8}$$

The nonlinear polarization is

$$\mathscr{P}^{NL}(t,z) = \frac{1}{2}[\mathscr{P}^{NL}_\omega(z)\exp(i(\omega t - kz)) + c.c.] \tag{2.9}$$

With the slowly varying envelope approximation employed

$$\frac{d^2E_\omega}{dz^2} \ll k\frac{dE_\omega}{dz}$$

for quasi-monochromatic waves in the sum-frequency mixing process ($\omega_1 = \omega_2+\omega_3$), the coupled wave equations (CWE) are obtained [3]

$$\begin{aligned}
\frac{\partial E_1}{\partial z} &= i\kappa_1 E_2 E_3\exp(i\Delta kz)\\
\frac{\partial E_2}{\partial z} &= i\kappa_2 E_1 E_3^*\exp(-i\Delta kz)\\
\frac{\partial E_3}{\partial z} &= i\kappa_3 E_1 E_2^*\exp(-i\Delta kz)
\end{aligned} \tag{2.10}$$

in which

$$\Delta k = k_1 - k_2 - k_3,\ \kappa_m = \frac{\mu_0\varepsilon_0\omega_m^2}{2k_m} = \frac{\omega_m\sqrt{\mu_0\varepsilon_0}}{n_m}d_{\text{eff}},\ m = 1,\ 2,\ 3$$

and d_{eff} is the effective nonlinear coefficient.

For SHG, these equations become

$$\begin{aligned}
\frac{\partial E_\omega}{\partial z} &= i\kappa_\omega E_{2\omega}E_\omega^*\exp(-i\Delta kz)\\
\frac{\partial E_{2\omega}}{\partial z} &= i\kappa_{2\omega}E_\omega^2\exp(i\Delta kz)
\end{aligned} \tag{2.11}$$

in which

$$\kappa_\omega = \frac{\omega\sqrt{\mu_0\varepsilon_0}}{n_\omega}d_{\text{eff}},\ \kappa_{2\omega} = \frac{2\omega\sqrt{\mu_0\varepsilon_0}}{n_{2\omega}}d_{\text{eff}},\ \Delta k = k_{2\omega} - 2k_\omega$$

Assume the nonlinear medium thickness along the wave propagation direction is L, and the pump light does not deplete,

$$E_\omega(0) = E_0,\ E_{2\omega} = 0,\ \frac{\partial E_\omega}{\partial z} = 0$$

Thus the second harmonic field amplitude at the other end of the medium is then [4]

$$E_{2\omega}(L) = i\kappa_{2\omega}E_0^2 L\mathrm{sinc}(\frac{\Delta kL}{2})\exp(i\frac{\Delta kL}{2}) \tag{2.12}$$

So then we know the second harmonic light intensity

$$I_{2\omega}(L) \propto d_{\mathrm{eff}}^2 I_0^2 L^2 \mathrm{sinc}^2(\frac{\Delta kL}{2}) \tag{2.13}$$

The second harmonic power dependence on the phase mismatch is shown in Fig. (2.1) (a). For the maximum conversion efficiency, the condition $\Delta k = 0$ should be fulfilled, which is called phase-matching. If the waves interact strongly, the non-depletion approximation will not be valid any more. For the phase-matched case ($\Delta k = 0$), the solution for plane waves in lossless media is [5]

$$\begin{aligned} I_{2\omega}(L) &= I_\omega(0)\tanh^2(\Gamma L) \\ I_\omega(L) &= I_\omega(0)\mathrm{sech}^2(\Gamma L) \end{aligned} \tag{2.14}$$

where

$$\Gamma = \frac{4\pi d_{\mathrm{eff}}\sqrt{I_\omega(0)}}{\sqrt{2cn_\omega^2 n_{2\omega}\varepsilon_0\lambda_\omega^2}},\ I_\omega(0) = \frac{cn_\omega\varepsilon_0}{2}E_\omega^2(0) \tag{2.15}$$

The conversion efficiency is then

$$\eta(L) = \frac{I_{2\omega}(0)}{I_\omega(0)} = \tanh^2(\Gamma L) \tag{2.16}$$

The solution given by Eqn. (2.14) is shown graphically in Fig. (2.1) (b), where the quantity L_N is defined as

$$L_N = 1/\Gamma \tag{2.17}$$

This is the simulation result under the plane wave approximation. In reality, the laser beams are usually Gaussian and the conversion efficiency cannot be so high as in Fig. (2.1) (b).

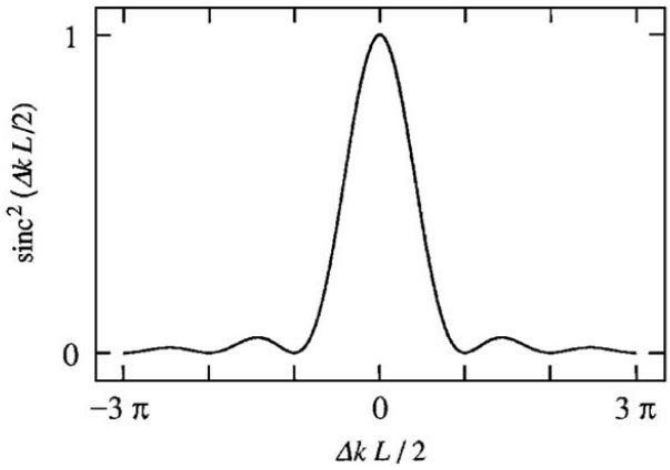

(a)

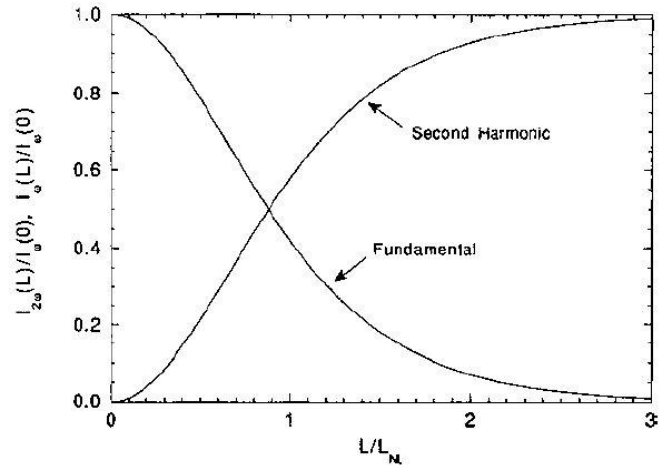

(b)

Figure 2.1: (a) Effects of wavevector mismatch on the efficiency of sum-frequency generation, reprinted from [3]. (b) Second harmonic and fundamental intensities as functions of crystal length and nonlinear interaction length for phase-matched SHG including pump depletion, reprinted from [5].

2.4 Phase-matching

Unlike the energy conservation relation, the phase-matching condition is not automatically satisfied. As a result, there is a need to eliminate or compensate the phase mismatch. Currently, there are two major methods, that is, the birefringent

phase-matching (BPM) and the quasi phase-matching (QPM).

The phase-matching condition $\Delta k = 0$ is often difficult to achieve because usually in the lossless ranges the material refractive index shows a normal dispersion.

For SFM $\omega_2 + \omega_3 = \omega_1$, the condition for a perfect collinear phase-matching

$$\frac{n_2\omega_2}{c} + \frac{n_3\omega_3}{c} = \frac{n_1\omega_1}{c} \tag{2.18}$$

cannot be satisfied. For SHG $\omega_2 = \omega_3 = \omega,\ \omega_1 = 2\omega$, the phase-matching condition is equivalent with

$$n(\omega) = n(2\omega) \tag{2.19}$$

Apparently, this is also impossible for a monotonic $n(\omega)$. However, as is shown in Fig. (2.2) when the nonlinear material is birefringent, the perfect phase-matching is possible. In BPM, the highest frequency $\omega_1 = \omega_2 + \omega_3$ is polarized in the direction

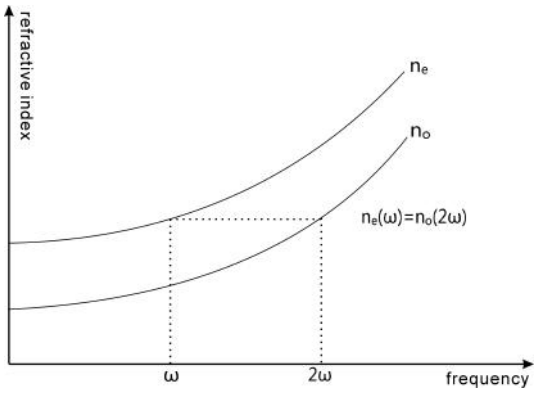

Figure 2.2: The refractive indices of the fundamental and second harmonic frequencies in a SHG case

which gives it the lower of the two possible refractive indices. As for the two lower frequencies ω_2 and ω_3, there are two choices for the polarization directions: the same or orthogonal [6].

The effective nonlinear coefficient d_{eff} can depend strongly on the propagation and polarization direction in the nonlinear crystal. And sometimes the largest nonlinearities cannot be used for most wavelengths as the dispersion in this case cannot be compensated. For example, d_{33} in KTP crystals cannot be used for BPM. It is even possible that the solution for the BPM direction in a material actually has no or insufficient nonlinearities. Furthermore, some nonlinear materials exhibit a very low birefringence in comparison with its dispersion, especially for short wavelengths near the absorption edge.

2.5 Quasi Phase-matching

There is a technique named quasi phase-matching for overcoming the disadvantages above, which was proposed by Armstrong *et al.* [7]. The idea is to change the phases of all interacting waves by π every coherence length $L_c = \pi/\Delta k$. As a result, the wavevector mismatch becomes (assume for SFM $\omega_1 = \omega_2 + \omega_3$)

$$\Delta k' = (k_1 + \frac{\pi}{L_c}) - [(k_2 + \frac{\pi}{L_c}) + (k_3 + \frac{\pi}{L_c})] = \Delta k - \frac{\pi}{L_c} = k_m - k_m = 0 \quad (2.20)$$

before the generated light power starts coupling back to the fundamental frequency, where k_m is the grating vector of the periodic structure (in this case it is the first order $k_1 = \Delta k$) and m is the QPM order. Twice the coherence length is called the grating period $\Lambda = 2L_c$. Practically, the phase mismatch is compensated by the grating vector of the periodic $\chi^{(2)}$ structure as shown in Fig. (2.3).

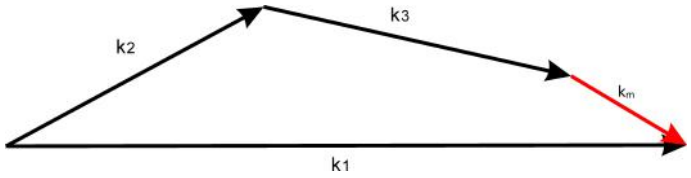

Figure 2.3: The phase-matching scheme of QPM, $\mathbf{k_m}$ is the grating vector of the periodic QPM structure.

One way to achieve this is known as periodical poling, which is convenient for ferroelectrics. In this technique, the orientation of the polar axis, usually the c-axis of the crystal, is inverted periodically as a function of position along the fundamental beam direction within the material, which can be done electrically.

In this project, the QPM crystals were mostly processed by periodical poling. So the spatial modulation of the nonlinearity can be expressed as

$$d(z) = d_{\text{eff}}\text{sgn}[\cos(2\pi z/\Lambda)] \quad (2.21)$$

This can also be described in terms of Fourier series

$$d(z) = d_{\text{eff}} \sum_{m=-\infty}^{\infty} G_m \exp(ik_m z) \quad (2.22)$$

where $k_m = 2\pi m/\Lambda$ is the magnitude of the QPM grating vector. And the coefficient G_m is

$$G_m = (2/m\pi)\sin(m\pi/2),\ m \in N_+ \quad (2.23)$$

One can assume that one of these Fourier components of $d(z)$ dominates because all other components have an average contribution of zero. The coupled wave equations

in this case are [3]

$$\begin{aligned}\frac{dE_1}{dz} &= \frac{2i\omega_1 d_Q}{n_1 c} E_2 E_3 \exp[i\Delta k_Q z] \\ \frac{dE_2}{dz} &= \frac{2i\omega_2 d_Q}{n_2 c} E_1 E_3^* \exp[-i(\Delta k_Q - 2k_m)z] \\ \frac{dE_3}{dz} &= \frac{2i\omega_3 d_Q}{n_3 c} E_1 E_2^* \exp[-i(\Delta k_Q - 2k_m)z]\end{aligned} \tag{2.24}$$

where d_Q is the nonlinear coupling coefficient

$$d_Q = d_{\text{eff}} G_m \tag{2.25}$$

and Δk_Q is the wavevector mismatch

$$\Delta k_Q = k_2 + k_3 - k_1 + k_m \tag{2.26}$$

In order to achieve QPM, Δk_Q must be zero, which is the momentum conservation condition for QPM. The period of the QPM crystal is

$$\Lambda = 2mL_c = 2m\pi/\Delta k \tag{2.27}$$

where $\Delta k = k_2 + k_3 - k_1$. In crystals with a 50% duty cycle, only the odd orders can be utilized for QPM, as the effective nonlinearity is zero for even orders.

Under the non-depletion approximation, the field amplitude of the second harmonic wave at the n-th domain is [5]

$$\begin{aligned}E_{2\omega,n}(z) =& \frac{-8\pi d_Q E_\omega^2}{n_{2\omega}\lambda_\omega \Delta k} \\ &\times \left\{(n-1) - i^n \exp\left(i\frac{\Delta k z}{2}\right) \sin\left[\frac{\Delta k z}{2} + (n-1)\frac{\pi}{2}\right]\right\}\end{aligned} \tag{2.28}$$

The comparison between the generated light intensities of non-phase-matching, perfect phase-matching and quasi phase-matching situations under non-depletion approximation is shown in Fig. (2.4).

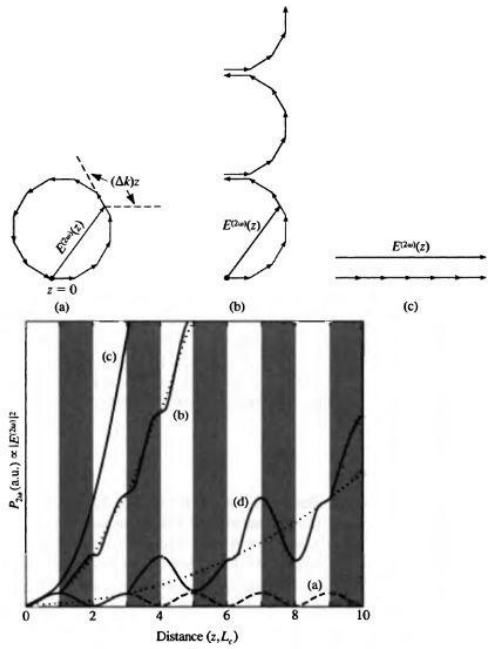

Figure 2.4: The vectorial second-harmonic phasor $E^{(2\omega)}(z)$ and its spatial evolution in (a) a non-phase-matched case, (b) quasi-phase-matched case, and (c) bulk birefringent phase-matching case ($\Delta k = 0$). (d) is the spatial evolution for quasi-phase-matched operation using the third-order. Adapted from [8]

Chapter 3

Ferroelectrics and KTP

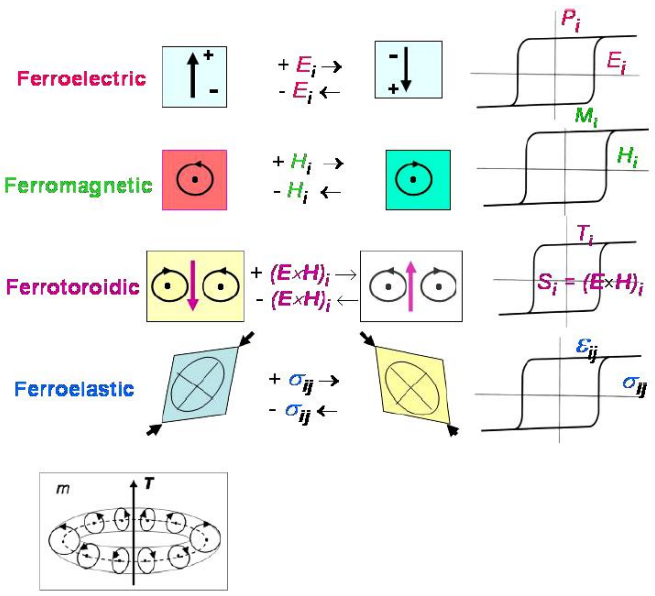

Figure 3.1: Schematic domain switching and hysteresis cycles of the four primary ferroics. The symmetry symbol used for the toroidal moment corresponds to the co-axial mirror plane cross-section of a toroid with an even number of windings (see inset). Adapted from [9].

In 1907, Weiss used the prefix "*ferro*" [10] for ferroic materials for the first time. So far we have four types of ferroics: ferromagnetics, ferroelectrics, ferroelastics and ferrotoroidics [11]. These four concepts of ferroics are shown in Fig. (3.1). Statistically, the word *ferroics* means the formation of *domains* upon a phase transition

from a high temperature *prototype* phase to a low-temperature low-symmetry *ferroic* phase divided by the Curie temperature T_c, with the appearance of an *order parameter* with at least two switchable equivalent energy states, where *domains* mean the regions with the same orientations of the order parameter (Fig. (3.2)) [12][9].

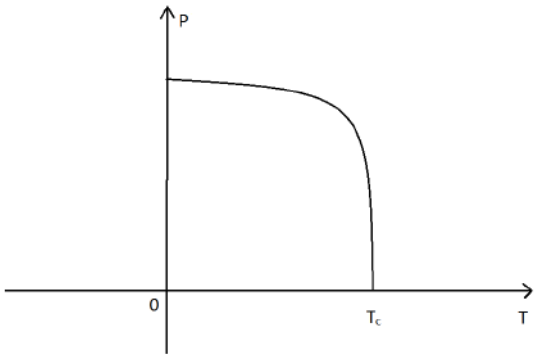

Figure 3.2: The phase transition (second-order) for ferroelectric materials. T_c is the Curie temperature.

In a linear medium, the polarization is proportional to the external electric field

$$\mathscr{P} = \varepsilon_0 \chi \mathbf{E} \tag{3.1}$$

However, for some materials, this response is not linear. Without external fields, there can still be spontaneous polarization. Some materials have a special response to external field, namely, the hysteresis loop (Fig. (3.1) (a)). A ferroelectric material is a material that exhibits a spontaneous electric polarization that can be reversed or reoriented by application of an electric field over some range of temperature [13].

3.1 Ferroelectric Domain Walls

In a ferroelectric material, the regions with the same orientations of the polarization vector are called *ferroelectric domains* and the boundaries between different domains are called *domain walls*. In my experiments, the domain walls utilized are called 180° domain walls, meaning the electric polarizations of the domains on the two sides of one domain wall are antiparallel and have two switchable equivalent energy states.

As is mentioned, *domain walls* are the boundaries between different domains. Due to defect localization by domain walls and domain wall pinning by defects,

domain walls are glassy systems with several *metastable* states [12], where there are more defects than in the bulk [14]. However, the coupling between domain walls and defects may hinder the domain wall motion when the crystal is under an external electric field in order to achieve polarization switching. [15]

Usually, domain walls are measured with atomic field microscopy (AFM), scanning electron microscopy, piezoelectric force spectroscopy and x-ray diffraction. However, it is rather difficult to obtain the exact value of the domain wall thickness which is often comparable with the resolution, e.g. the nominal apex radius of the tip of AFM (20-50 nm) and in KTP, the domain wall thickness is about 20-80 nm [16].

3.2 Crystal Symmetry

A solid is a large collection ($\sim 10^{23}$) of atoms which attract each other to form a structure of a definite shape and volume, with characteristic structural rigidity. A crystalline solid is a material whose atoms have a regular arrangement that exhibits translational symmetry [17]. Many material properties are determined by the crystal symmetry, e.g. piezoelectricity, pyroelectricity and ferroelectricity. Piezoelectric crystals have the following property: if stress is applied along certain directions in the crystals, they develop an electric polarization. Conversely, when an electric field is applied along certain directions in a piezoelectric crystal, the crystal is strained [13]. Whereas pyroelectricity means heat-generated electric charges or charge-generated heat [18].

There are seven crystal systems and 32 point group symmetries for crystals. In the international notation [17], the n-fold rotational symmetry is denoted as n and $\bar{n}$ is the n-fold rotoinversion symmetry. n/m means means an n-fold rotation axis with a perpendicular (horizontal) mirror plane. np depicts an n-fold rotation axis with p perpendicular twofold axes. $\bar{n}p$ denotes an n-fold rotoinversion axis with p perpendicular twofold axes. nm means a rotation axis with a parallel (vertical) mirror plane. $\bar{n}m$ represents a rotoinversion axis with a parallel mirror plane. A rotation axis with a mirror perpendicular (horizontal) plane and mirror parallel (vertical) planes is denoted as n/mm or $(n/m)m$. Alternatively the Schönflies notation [19] can be used (Tab (3.1)). Amongst these 32 point groups, 11 are centrosymmetric and 21 are noncentrosymmetric. The 11 centrosymmetric classes are nonpolar, thus they do not have a spontaneous polarization. One of the 21 classes have other symmetry elements resulting in non-piezoelectricity and the rest 20 are piezoelectric. 10 out of the 20 classes have a spontaneous polarization, namely, 1, 2, m, $2mm$, 4, $4mm$, 3, $3m$, 6, $6mm$ [13]. They are pyroelectric, some of which are ferroelectric. As we know second-order nonlinearity also requires noncentrosymmetry, this makes it possible to find both $\chi^{(2)}$ and ferroelectricity in the same material, which makes QPM viable.

The order of symmetry together with the optical group of different crystal systems are shown as in Tab. (3.2).

Table 3.1: Schönflies and international symbols for point groups, and permissible point groups for each crystal system

Crystal system	International symbol	Schönflies symbol
Triclinic	1	C_1
	$\bar{1}$	C_i
Monoclinic	2	C_2
	m	C_{1h}
	$(2/m)$	C_{2h}
Orthorhombic	222	D_2
	$2mm$	C_{2v}
	$(2/m)(2/m)(2/m)$	D_{2h}
Tetragonal	4	C_4
	$\bar{4}$	S_4
	$(4/m)$	C_{4h}
	422	D_4
	$4mm$	C_{4v}
	$\bar{4}2m$	D_{2d}
	$(4/m)(2/m)(2/m)$	D_{4h}
Trigonal	3	C_3
	$\bar{3}$	C_{3i}
	32	D_3
	$3m$	C_{3v}
	$\bar{3}(2/m)$	D_{3d}
Hexagonal	6	C_6
	$\bar{6}$	C_{3h}
	$(6/m)$	C_{6h}
	622	D_6
	$6mm$	C_{6v}
	$\bar{6}m2$	D_{3h}
	$(6/m)(2/m)(2/m)$	D_{6h}
Cubic	23	T
	$(2/m)\bar{3}$	T_h
	432	O
	$\bar{4}3m$	T_d
	$(4/m)(\bar{3})(2/m)$	O_h

3.3 Potassium Titanyl Phosphate

Potassium titanyl phosphate ($KTiOPO_4$, KTP) is one of the basic nonlinear optical crystals which has widely been used in frequency conversion devices since 1980s [20], due to its high second-order susceptibility, very low onset power threshold, high power conversion efficiency and high threshold to laser-induced damage. In

Crystal System	*Optical Group*	*Order of Symmetry*
Triclinic	Biaxial	Very Nonsymmetric
Monoclinic	Biaxial	
Orthorhombic	Biaxial	
Tetragonal	Uniaxial	Increasing
Trogonal (Rhombohedral)	Uniaxial	
Hexagonal	Uniaxial	
Cubic	Optically Isotropic	Very Symmetric

Table 3.2: The seven basic crystal systems. Reprinted from [18].

1890, Ouvrard published the synthesis of KTP [21] but until 1976 it was not introduced as a nonlinear optical material [22]. The crystal structure of KTP was determined for the first time by Tordjman *et al.* in 1974 [23]. Rb-doped potassium titanyl phosphate, $K_xRb_{1-x}TiOPO_4$ (RKTP), was introduced as an excellent nonlinear optical material together with KTP in 1976 [22]. Amongst the QPM crystals reported in this thesis, some are KTP and others are RKTP which have 0.3% Rb^+ ions instead of K^+ ions. RKTP crystals with a low Rb^+ concentration have very similar optical properties with KTP crystals, so the usage of RKTP does not introduce new uncertainties to CSHG. However, RKTP crystals have a significantly lower ionic conductivity compared to KTP, leading to a much better grating structure after electric field periodic poling[24]. There are two major methods of KTP crystal growth: hydrothermal and flux [21].

KTP belongs to the point group $2mm$ and is a positive biaxial crystal, with an angle between two optic axes $2V_z = 37.4°$ at $\lambda = 546.1$ nm [25]. The density is 2.945 g/cm^3 [26][27]. KTP belongs to the point group $2mm$ and the acentric orthorhombic space group $Pna2_1$ [22]. The crystalline axes a, b and c correspond to the dielectric axes X, Y and Z, respectively. The lattice constants are

$$a = 12.814 \text{ Å},\ b = 6.404 \text{ Å},\ c = 10.616 \text{ Å [28]}$$

In KTP, each unit cell contains two groups of crystallographically nonequivalent $KTiOPO_4$ molecules. In each unit cell there are two nonequivalent Ti lattice sites Ti(1) and Ti(2), as well as K(1) and K(2), P(1) and P(2), and O(1),O(2),...O(10). Ti and O form the distorted TiO_6 octahedra, and P and O form the PO_4 tetrahedra. The distorted TiO_6 octahedra in c-axis direction bridge the PO_4 tetrahedra to form a $\cdots$-PO_4-TiO_6-PO_4-$\cdots$ lattice array. The potassium ions are located in

the channels of the framework along the $c-$axis. K^+ is eight-coordinated(K(1)) or nine-coordinated(K(2)) [29]. In RKTP, the Rb^+ ion can only occupy the K(2) site at a low concentration [30]. During the electric field poling, the potassium cations change their sites from K(1) to K(2) or from K(2) to K(1). The schematic view of KTP crystal structure along $b-$axis near a domain wall is shown in Fig. (3.3).

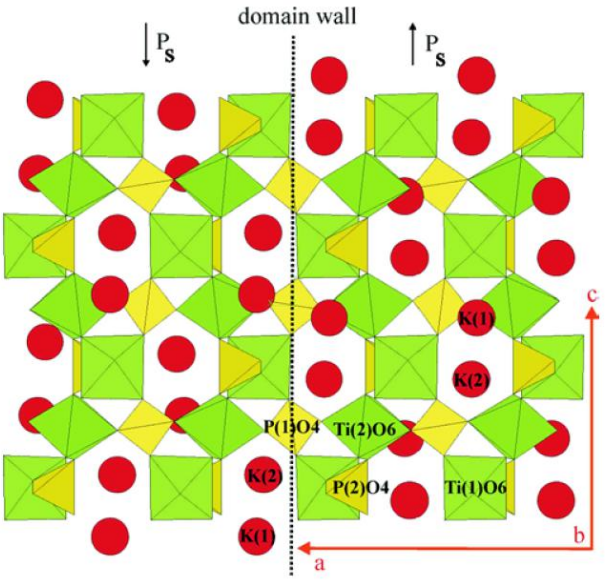

Figure 3.3: Schematic view of a domain wall (dotted line) perpendicular to the a axis passing through the atom P(1). Reprinted from [31].

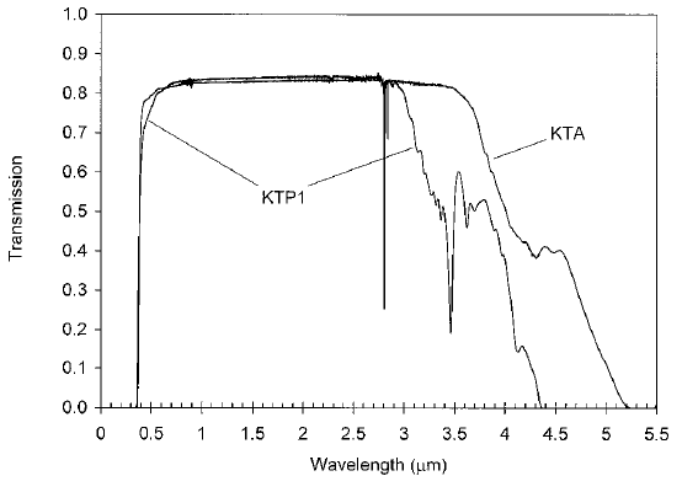

Figure 3.4: Transmission window for KTP1 and KTA in the $E \| z$ polarization direction. Reproduced from [35].

3.4 Optical Properties of KTP

The bulk second-order nonlinearity tensor of KTP is [32][24]

$$\mathbf{d} = \begin{bmatrix} 0 & 0 & 0 & 0 & d_{15} & 0 \\ 0 & 0 & 0 & d_{24} & 0 & 0 \\ d_{31} & d_{32} & d_{33} & 0 & 0 & 0 \end{bmatrix} \tag{3.2}$$

where theoretically $d_{15} = d_{31}$ and $d_{24} = d_{32}$. The signs of KTP second-order nonlinear coefficients are all the same [33] and the absolute values of them are [34]

$$\begin{aligned} d_{15}(1064\text{ nm}) &= 1.9 \pm 0.1\text{ pm/V} \\ d_{24}(1064\text{ nm}) &= 3.7 \pm 0.2\text{ pm/V} \\ d_{31}(1064\text{ nm}) &= 2.2 \pm 0.1\text{ pm/V} \\ d_{32}(1064\text{ nm}) &= 3.7 \pm 0.2\text{ pm/V} \\ d_{33}(1064\text{ nm}) &= 14.6 \pm 0.7\text{ pm/V} \end{aligned} \tag{3.3}$$

where the wavelength indicates the wavelength of the fundamental beam.

KTP has a transmission range from 0.35 μm to 4.5 μm [22]. The transmission spectrum of KTP is shown together with potassium titanyl arsenate (KTA) in Fig. (3.4).

In many cases, the refractive index is of great importance concerning practical calculations, such as reflectivity, dispersion and conversion efficiency. According to

Fan *et al.*, the infrared-corrected Sellmeier equation for n_z in the spectral range $[0.4047, 1.064]\mu$m is [36] (λ in μm)

$$n_z^2 = 2.25411 + \frac{1.06543\lambda^2}{\lambda^2 - 0.05486} - 0.02140\lambda^2 \tag{3.4}$$

The temperature correction for the refractive indices of flux-grown KTP for $\lambda = 0.502 \sim 1.129\mu$m is ($\lambda$ in μm) [37]

$$\begin{aligned}
\frac{dn_x}{dT} &= \left(\frac{1.427}{\lambda^3} - \frac{4.735}{\lambda^2} + \frac{8.711}{\lambda} + 0.952\right) \times 10^{-6}\mathrm{K}^{-1} \\
\frac{dn_y}{dT} &= \left(\frac{4.269}{\lambda^3} - \frac{14.761}{\lambda^2} + \frac{21.232}{\lambda} - 2.133\right) \times 10^{-6}\mathrm{K}^{-1} \\
\frac{dn_z}{dT} &= \left(\frac{12.415}{\lambda^3} - \frac{44.414}{\lambda^2} + \frac{59.129}{\lambda} - 12.101\right) \times 10^{-6}\mathrm{K}^{-1}
\end{aligned} \tag{3.5}$$

3.5 Electric Field Periodic Poling

For (R)KTP crystals, the most common polarization switching method is electric field periodic poling [24], where an external electric field is applied along the polar axis to switch the electric polarization of ferroeletric crystals periodically. Domain kinetics during electric field periodic poling are given in six stages as is shown in Fig. (3.5).

The schematic of the poling setup is shown in Fig. (3.6), where usually the pattern on the *c*- facet is written with the help of photolithography. Usually, electrodes are made periodic to achieve the periodic grating structures in the crystal. In Fig. (3.5 (a) and (b)), the domain nucleation and tips are due to the geometry of electrodes.

Furthermore, the pattern on the QPM crystals can be more diverse than merely parallel stripes. Multiple grating, fan-out grating, or even 2D nonlinear photonic structures are also possible.

Although the goal of electric field poling is to obtain a uniform QPM grating structure with desired grating period and desired duty cycle in the case of one-dimensional parallel stripe grating structures shown as in Fig. (3.5 (f)), in reality, it is very difficult to fulfil, because there are so many factors that could bring large deviations, such as crystal homogeneity, ionic conductivity, defect concentration, poling temperature, electric pulse shape and so forth [24]. Particularly, for sub-μm period crystals, the poling quality control is even more challenging. Besides, in the poling process of sub-μm period crystals, the domain tip propagation may not be able to reach the *c*+ facet as in Fig. (3.5 (c)). Usually, techniques like atomic force microscopy, piezoelectric force microscopy, scanning electron microscopy and selective chemical etching are used for monitoring the poling quality. However, they are all limited to surface or thin films. Also, some are even destructive. Forward SHG and electro-optic effect could also be used, however, they only show

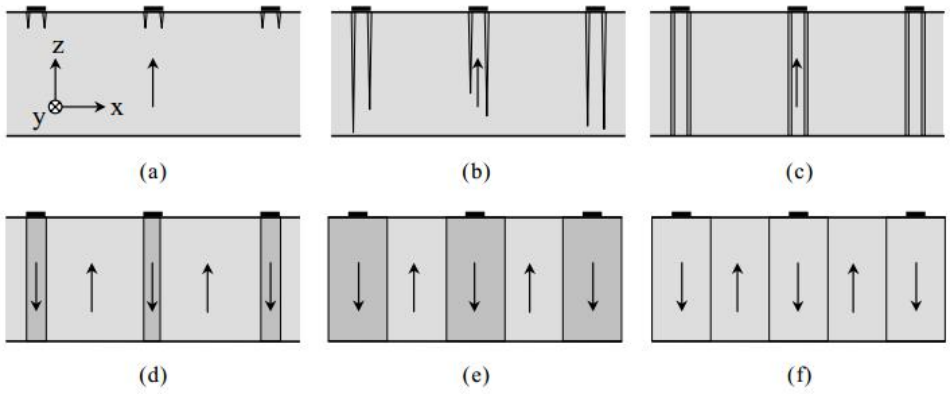

Figure 3.5: The six stages of domain kinetics during electric field periodic poling. (a) Domain nucleation at the electrode edges. (b) Domain tip propagation toward the opposite face of the crystal. (c) Termination of the tip at the opposite side of the crystal. (d) Rapid coalescence under the electrodes. (e) Propagation of the domain walls out from under the electrodes. (f) Stabilization of the new domains, reprinted from [38].

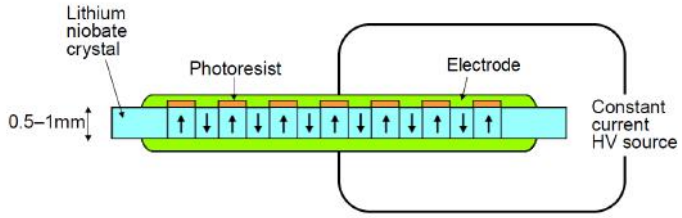

Figure 3.6: The schematic of the poling setup on a lithium niobate crystal. Adapted from [39].

the average situation over all domains. So a nondestructive and in-deep domain (wall) characterization method which only tests a few domains is needed in this case. Čerenkov SHG is an option.

Chapter 4

Čerenkov Phase-matching

Čerenkov phase-matching refers to longitudinal phase-matching, in which only the wave vector components parallel with the interface are matched. (Fig. (4.1) (a)) The theory of Čerenkov phase-matching (CPM) was proposed by Bloembergen and Pershan in 1962 [40], which is also called "nonlinear Snell's law" [5]. For example, for a Čerenkov SFM at crystal boundaries or waveguides $\omega_1 + \omega_2 = \omega_3$,

$$\frac{n_1 \sin\theta_1}{\lambda_1} + \frac{n_2 \sin\theta_2}{\lambda_2} = \frac{n_3 \sin\theta_3}{\lambda_3} \tag{4.1}$$

where n_j, θ_j and λ_j ($j = 1, 2, 3$) are the refractive index, incident/refractive/reflective angle and wavelength for the i-th wave. Čerenkov second harmonic generation was observed in experiments by Zembrod *et al.* [41] in 1969 and the nonlinear Fresnel equations were developed by Bloembergen *et al.* [42].

4.1 Theories for Čerenkov Phase-matching

CPM was first observed at the boundary of nonlinear crystal and the interface of waveguide. The formalism of nonlinear refraction and reflection works well for these two situations, as the refractive indices for the same wavelength on two sides of the interface are different.

Consider a second harmonic process $2\omega = \omega + \omega$. The wave numbers of the fundamental, "reflected" and "refracted" beams are k_ω, $k_{2\omega}$ and $k'_{2\omega}$, respectively; the refractive indices are n_ω, $n_{2\omega}$ and $n'_{2\omega}$, respectively; the wavelength of the fundamental beam is λ (Fig. (4.1) (b)).

From nonlinear Snell's law we then have [5]

$$\frac{n_\omega \cos\alpha}{\lambda} + \frac{n_\omega \cos\alpha}{\lambda} = \frac{n'_{2\omega} \cos\beta}{0.5\lambda} = \frac{n_{2\omega} \cos\gamma}{0.5\lambda} \tag{4.2}$$

where α, β and γ are the angles between the interface and the fundamental, "reflected", and the "refracted" beams, respectively. This is equivalent with the lon-

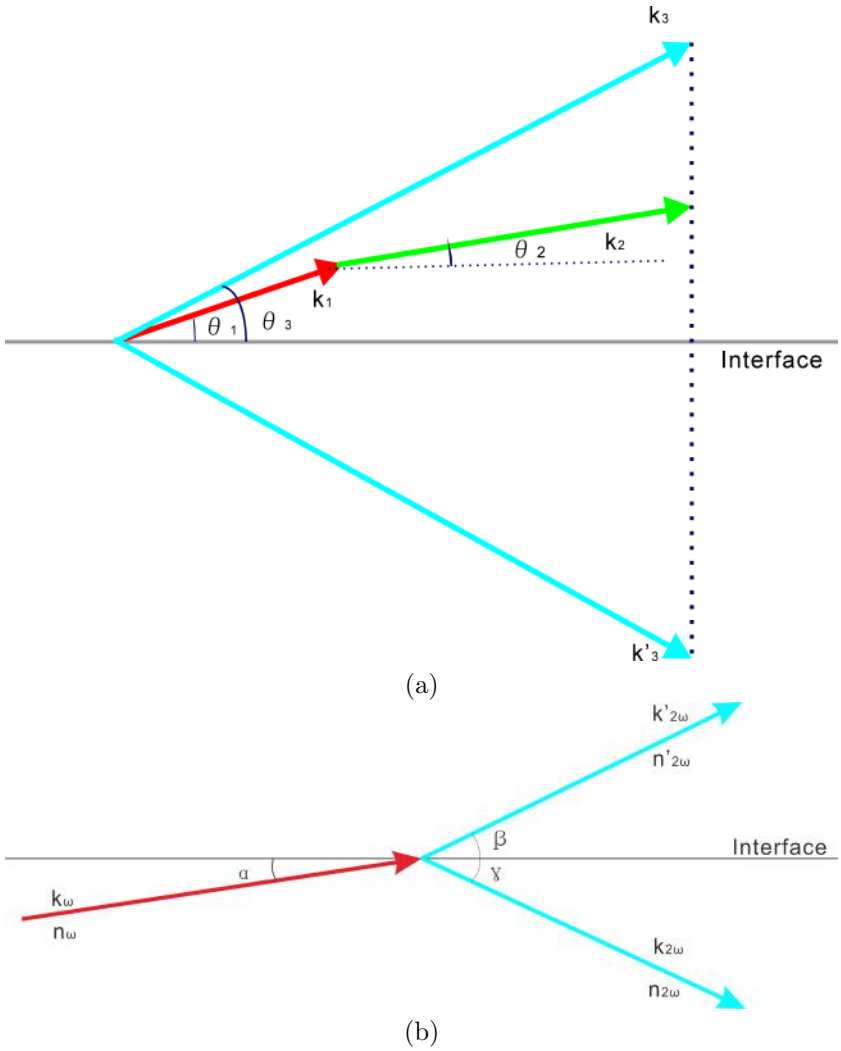

Figure 4.1: (a) The schematic for Čerenkov phase-matching, the case of SFM; (b) The Čerenkov phase-matching at the interface between two different layers of materials

gitudinal phase-matching condition

$$2k_\omega \cos\alpha = k'_{2\omega} \cos\beta = k_{2\omega} \cos\gamma \tag{4.3}$$

According to Bloembergen and Pershan [40], this is a consequence of the continuity of the tangential components of the electric fields at the interface. In waveguides,

the quantity $n_\omega \cos\alpha$ is often called the effective refractive index N_ω [5]. If we define the velocity $V_\omega = c/N_\omega$ and the phase velocity of the two second harmonic waves $v'_{2\omega}$ and $v_{2\omega}$, then the Čerenkov angle can be expressed in terms of phase velocities

$$\begin{aligned} \cos\beta &= v'_{2\omega}/V_\omega \\ \cos\gamma &= v_{2\omega}/V_\omega \end{aligned} \tag{4.4}$$

where the famous Čerenkov radiation condition $V_\omega > v'_{2\omega}$ and $V_\omega > v_{2\omega}$ has to be fulfilled.

Fragemann [43] *et al.* confirmed that Čerenkov second harmonic generation also exists at ferroelectric domain walls. However, in this case, the nonlinear Snell's law formalism cannot be applied. The reason is that the material on both sides of the ferroelectric domain walls is the same. The physical origin of Čerenkov phase-matching of ferroelectric domain walls is still unclear. Currently, there are several theories based on reciprocal lattice vector [44][45][46], local field enhancement [47][43][12], defect scattering [14][48] and so forth. Currently, in most papers the bulk Čerenkov phase-matching is absent. However, some authors have claimed otherwise from their experiments [49][50], yet the alleged bulk CSHG signals could be from the domain walls of a multidomain crystal [51], which was not investigated.

According to these theories, there are two key aspects in the Čerenkov phase-matching of ferroelectric domain walls: the phase-matching condition and the $\chi^{(2)}$ enhancement. They can be sorted into two categories. The first one is that there is also CPM in the bulk but without the enhancement as at the interfaces the interaction is too weak; the second is that CPM can only happen at the interfaces where the transverse phase mismatch is compensated by the boundary condition and the absence of the nonlinearity enhancement is not the reason why CPM cannot be detected from the bulk.

If we employ the second one, the Čerenkov angle can be calculated from the wave nature of light. I assume that the nonlinear polarization is confined within the domain wall, for the SFM process $\omega_3 = \omega_1 + \omega_2$, the whole CPM process can be divided into two parts: the propagation of the nonlinear polarization as a wave(AD in Fig. (4.2)), and the propagation of the generated light (DB in Fig. (4.2)). I assume the wave vectors of ω_j ($j = 1,\ 2,\ 3$) are k_j, the electric field amplitudes are E_j and the domain walls are along $x-$axis. The nonlinear polarization is then

$$\begin{aligned} \mathscr{P}^{NL} &= \varepsilon_0 \chi^{(2)} E_1 E_2 \exp[i(\mathbf{k_1} + \mathbf{k_2}) \cdot \mathbf{r} - i(\omega_1 + \omega_2)t] \\ &= \mathscr{P}_0^{NL} \exp[i(\mathbf{k_1} + \mathbf{k_2}) \cdot \mathbf{e_x} - i(\omega_1 + \omega_2)t] \end{aligned} \tag{4.5}$$

where $\mathbf{e_x}$ is the unit vector along $x-$axis, and $P_0 = \varepsilon_0 \chi^{(2)} E_1 E_2$. And the electric field of the generated wave is

$$E_3 = E_{3,0} \exp[i\mathbf{k_3} \cdot \mathbf{e_x} - i\omega_3 t] \tag{4.6}$$

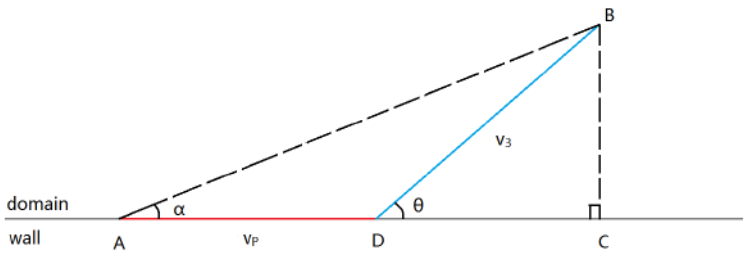

Figure 4.2: The Čerenkov phase-matching explained with wave optics

As a result, the phase velocities of the nonlinear polarization and the generated wave are

$$\begin{aligned} v_{\mathscr{P}} &= (\omega_1 + \omega_2)/(k_{1,x} + k_{2,x}) \\ v_3 &= \omega_3/(k_{3,x}) \end{aligned} \tag{4.7}$$

in which $k_{j,x}$ $(j = 1,\ 2,\ 3)$ is the projection of the wave vector onto $x-$axis, with a frequency ω_j. I assume $AC = a,\ BC = b$, so the total travel time T from A to B is then

$$T = \int_A^D \frac{ds}{v_{\mathscr{P}}} + \int_D^B \frac{ds}{v_3} = \frac{a - b\cot\theta}{v_{\mathscr{P}}} + \frac{b}{v_3 \sin\theta} \tag{4.8}$$

According to Fermat's Principle, when

$$\delta T/\delta\theta = 0 \tag{4.9}$$

we have the stationary solution, i.e. the constructive interference path or the beam path. Thus, we have

$$\cos\theta = \frac{v_3}{v_{\mathscr{P}}} \tag{4.10}$$

which is equivalent with

$$k_{1,x} + k_{2,x} = k_{3,x} = k_3 \cos\theta \tag{4.11}$$

This represents the condition for longitudinal phase-matching.

Chapter 5

Experiments

5.1 Introduction

Sheng *et al.* developed a novel method of domain characterization by combining confocal laser scanning microscopy and Čerenkov SHG at domain walls in ferroelectric materials [52] (Fig. (5.1)). This method is both nondestructive and applicable for in-depth QPM structure investigation. The idea is similar with the conventional confocal laser scanning microscopy but the signal is CSHG light, not fluorescence light. Since CSHG could only be generated from ferroelectric domain walls in the crystal bulk, the ferroelectric domain walls are visualized three-dimensionally. However, the method can only be applied to the polar direction for z-cut crystals as the spherical aberration of confocal microscopy is too large for "thicker" crystals, and the Rayleigh range is very short as the pump beam is focused.

In my experiments, all the samples are already chemically etched and I would like to preserve the etching patterns for reference, therefore, the polar surfaces are not suitable for probing with the laser beam. Furthermore, I want to get a rough evaluation of the crystal period (equivalently, the domain wall density) distribution in sub-μm period crystals along the polar direction without slicing crystals into thin pieces. To achieve this goal, I utilized the Čerenkov SHG at the domain walls in a modified scheme:

> First, the laser beam is along *b*-axis, for the polar surfaces are etched as a reference.
>
> Second, the laser beam is loosely focused so that the *mean* value of the period distribution across a relatively large volume in the crystal could be obtained in one single shot.
>
> Third, the largest nonlinear coefficient in KTP d_{33} is used and thus the pump light intensity requirement is lowered. As a result, a CW laser works well as a pump laser light source.

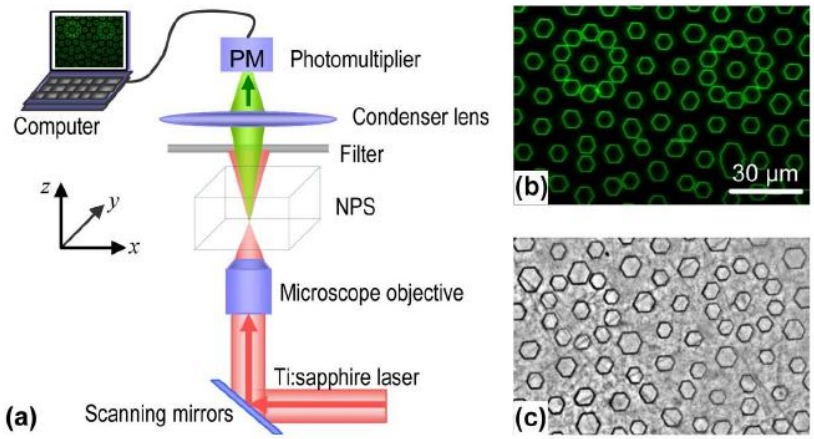

Figure 5.1: (a) Schematic of Sheng's experimental setup; (b-c) Images of the inverted domain pattern of a 2D quasi-periodic NPS obtained via (b) Čerenkov SHG inside the NPS and (c) optical microscopy after selective etching of the NPS surface, reprinted from [52].

5.2 Experimental Setup

The schematic figure and the photograph of the experimental setup are shown in Fig. (5.2). The laser light comes from a CW Ti: Sapphire laser (Spectral Physics Model 3900S, pumped by a 532 nm diode-pumped solid state laser), and is then transmitted through the glass plate where about 14.7% of the total power is reflected towards the first powermeter PM1 (Melles Griot 13PEM001 broadband power/energy meter). The transmitted beam is loosely focused by the lens L1 (f=100 mm) into the crystal on the translation stage. The two divergent beams of Čerenkov second harmonic are focused by the two lenses L2 and L3 with the same focal length (f=30 mm). One branch passes the filter F1 (two pieces of blue bandpass filters, Newport FSQ-BG40) and is observed by a CCD camera (Thorlabs), the other passes the filter F2 (one piece of the Newport FSQ-BG40 filter) and is collected by a very sensitive (resolution: 1 nW) powermeter PM2 (Thorlabs PM100D, with the sensor S130C).

The CCD camera is used for monitoring the beam spot shape to make sure the fundamental beam is probing the right region within the crystal and there is no total internal reflection. It is more sensitive than the powermeter PM2 but its dynamic range is much lower.

As the fundamental beam is Gaussian and the surface is selectively etched, I cannot directly measure at the polar surface. Instead, I measure the CSHG power from the regions about 50-100 μm below, so that the pump beam is not disturbed

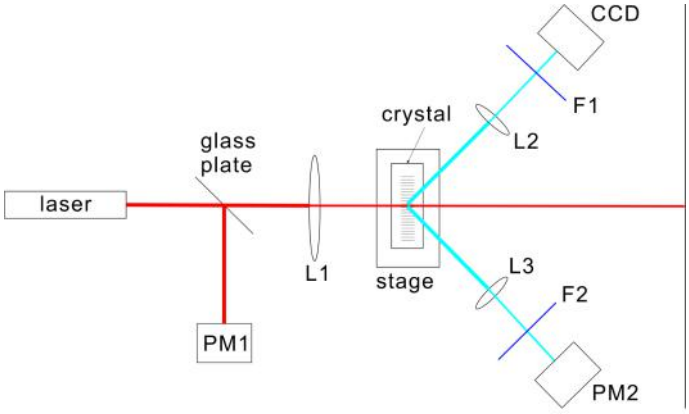

(a)

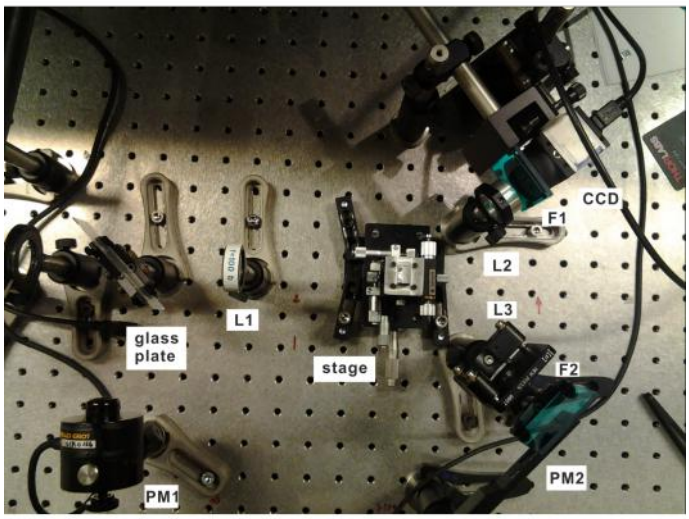

(b)

Figure 5.2: (a) The schematic of the experimental setup. (b) The photograph of the experimental setup.

by the polar surfaces of the crystal. If the pump beam is launched too close to the polar surfaces, part of the beam within the Rayleigh range will fall outside the crystal.

5.3 Čerenkov SHG with Gaussian Beams

The simplest model for the Čerenkov SHG is the plane wave approximation. Apparently, this is not applicable for my experiments as the pump beam is a focused Gaussian beam, the confocal parameter of which is of the magnitude of a few millimeters. As a result, we shall employ the theory of parametric interaction of focused Gaussian light beams by Boyd and Kleinman [53].

Consider a PPKTP crystal placed on the translation stage. The laboratory coordinate axes and the crystallographic axes are x, y, z and a, b, c, respectively. In my experiments, the x, y, z axes are identical with the respect a, b, c axes. The beam is launched along the y direction, the domain walls are in the yoz plane, and the origin $x = y = z = 0$ is at the point where the fundamental beam enters the crystal. Fig. (5.3) shows the configuration of the light beam and the crystal.

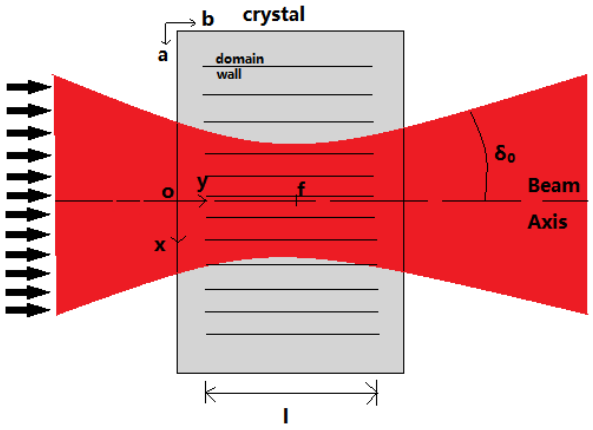

Figure 5.3: The experimental setup. The laboratory and crystallographic axes are parallel with the crystal edges.

In this "heuristic" model, the reflection is not considered for simplicity. The double-refraction for the extraordinary waves is $\mathrm{d}x/\mathrm{d}y = \tan\rho \approx \rho$. Since in my experiments I use the nonliearity d_{33} and the beam axis is the b axis, the quantity ρ is zero. The beam focus is at $y = f$. The minimum beam radius, confocal parameter, diffraction half-angle and fundamental wave number are w_0, b, δ_0 and k_1, respectively. They satisfy such relationships

$$w_0^2 k_1 = b \tag{5.1}$$

$$\delta_0 = k w_0 / b = 2/w_0 k_1 = 2/(b k_1)^{1/2} \tag{5.2}$$

These parameters are for the beam in the crystal. The parameters in the air are confocal parameter b', diffraction angle δ_0', wave number k_1', beam radius w_0' and focal position f'. If the crystal refractive index for the fundamental frequency is n_1,

$$b = n_1 b', \quad \delta_0 = \delta_0'/n_1, \quad k_1 = k_1' n_1, \quad w_0 = w_0', \quad f = f' n_1 \tag{5.3}$$

Along a specific light ray, there are two special points: the source point (x', y', z') and the observation point (x, y, z).

For the bulk nonlinear material model, the second-order nonlinearity component d_{33} is constant everywhere within the crystal. Whereas for the periodically poled KTP (PPKTP) crystals in my experiments, the sign of d_{33} changes periodically. As a result, the nonlinearity d_{33} is spatially modulated by a function $M(x')$:

$$d(x') = d_{33} M(x') \tag{5.4}$$

$$M(x') = \begin{cases} 1 & m\Lambda/2 + x_0' < x' \le (m+1)\Lambda/2 + x_0' \\ -1 & (m+1)\Lambda/2 + x_0' < x' \le (m+2)\Lambda/2 + x_0' \end{cases}, \ m \in Z \tag{5.5}$$

where x_0' is the random position offset and Λ is the crystal grating period. The nonlinear coefficient $d(x')$ is shown in Fig. (5.4).

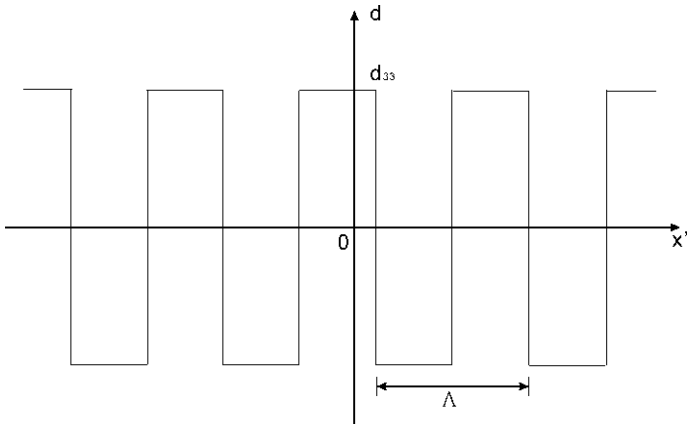

Figure 5.4: The spatial modulated nonlinear coefficient $d(x')$

The electric field amplitude of the fundamental beam can be expressed as

$$\begin{aligned} \mathbf{E}_1(x', y', z') =& \mathbf{E}_0[1/(1 + i\tau')] \exp(ik_1 y') \\ & \times \exp[-(x'^2 + z'^2)/w_0^2(1 + i\tau')] \exp(-\frac{1}{2}\alpha_1 y'), \end{aligned} \tag{5.6}$$

where $\tau' = 2(y' - f)/b$ and α_1 is the absorption coefficient for the fundamental frequency. The nonlinear polarization is

$$\begin{aligned}\mathscr{P}(x', y', z') = \mathscr{P}_0[1/(1 + i\tau')^2] \exp(2ik_1 y' - \alpha_1 y') \\ \times \exp[-2(x'^2 + z'^2)/w_0^2(1 + i\tau')]B(y')\end{aligned} \tag{5.7}$$

where

$$\begin{aligned}B(y') = 1 \qquad 0 \le y' \le l \\ = 0 \qquad otherwise\end{aligned} \tag{5.8}$$

Thus, we have the coupled wave equation for the second harmonic wave

$$\begin{aligned}\frac{\mathrm{d}E_2(x', y', z')}{\mathrm{d}y'} &= (2\pi i\omega_2/cn_2)\mathscr{P}_x(x', y', z') \exp(-ik_2 y') \\ &= (2\pi i\omega_2/cn_2)[\mathscr{P}_{0x}/(1 + i\tau')] \\ &\times \exp(i\Delta k y' - \alpha_1 y') \cdot \{[1/(1 + i\tau')] \\ &\times \exp[-2(x'^2 + z'^2)/w_0^2(1 + i\tau')]\}\end{aligned} \tag{5.9}$$

in which

$$\mathscr{P}_{0x} = d(x')E_0^2 = (16P_1/n_1 cw_0^2)d(x') \tag{5.10}$$

where P_1 is the pump power of the fundamental beam. Under the non-depletion assumption, E_0 and P_1 are both constants. According to Boyd and Kleinman [53], the part within the curly brackets remains invariant after the integration. As a result, the second harmonic field amplitude in the bulk is then

$$\begin{aligned}E_2(x', y', z') = \frac{2\pi i\omega_2 \mathscr{P}_{0x}(x')}{cn_2} \int_0^l \mathrm{d}y' \frac{\exp(-\alpha y' + i\Delta k y')}{1 + i\tau'} \\ \left\{\frac{1}{1 + i\tau'} \exp\left(-\frac{2(x'^2 + z'^2)}{w_0^2(1 + i\tau')}\right)\right\} \times \exp(-\frac{1}{2}\alpha_2 l + 2ik_1 y')\end{aligned} \tag{5.11}$$

where

$$\alpha = \alpha_1 - \frac{1}{2}\alpha_2 \tag{5.12}$$

and α_2 is the absorption coefficient for the second harmonic wave. I assume the Čerenkov SHG signal can only be generated at domain walls. If we define a modulation function $C(x')$,

$$C(x') = \begin{cases} 1 & -a/2 + m\Lambda/2 + x'_0 \le x' \le a/2 + m\Lambda/2 + x'_0 \\ 0 & a/2 + m\Lambda/2 + x'_0 < x' < -a/2 + (m + 1)\Lambda/2 + x'_0 \end{cases} \tag{5.13}$$

where a is the domain wall thickness and $m \in Z$. The electric field of the Čerenkov second harmonic wave will then be modulated by the function $C(x')$ (Fig. (5.5)).

$$\begin{aligned}E_2(x', y', z') = \frac{2\pi i\omega_2 \mathscr{P}_{0x}(x')}{cn_2} \int_0^l \mathrm{d}y' \frac{\exp(-\alpha y' + i\Delta k y')}{1 + i\tau'} \\ \left\{\frac{1}{1 + i\tau'} \exp\left(-\frac{2(x'^2 + z'^2)}{w_0^2(1 + i\tau')}\right)\right\} \times \exp(-\frac{1}{2}\alpha_2 l + 2ik_1 y')C(x')\end{aligned} \tag{5.14}$$

Again, according to Boyd and Kleinman, the electric field in the far field can be

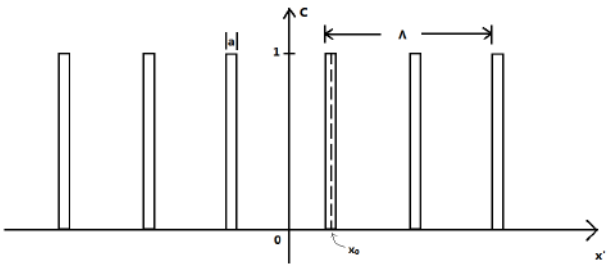

Figure 5.5: The function $C(x')$

expressed in terms of the observation coordinate

$$E_2(x,y,z) = \frac{2\pi i\omega_2 \mathscr{P}_{0x}(x')}{cn_2}\int_0^l \mathrm{d}y' \frac{\exp(-\alpha y' + i\Delta k y')}{1+i\tau'} \left\{\frac{1}{1+i\tau}\exp\left(-\frac{2((x-\rho(l-y'))^2+z^2)}{w_0^2(1+i\tau)}\right)\right\} \times \exp(-\frac{1}{2}\alpha_2 l + 2ik_1 y)C(x') \tag{5.15}$$

where

$$\begin{aligned} x' &= x-\rho(y-y') \qquad 0\le y\le l \\ x' &= x-\rho(l-y') \qquad y>l \\ z' &= z \\ \tau &= 2(y-f)/b \end{aligned} \tag{5.16}$$

The angle ρ is the double refraction angle for fundamental frequency. Employing the far-field approximation $1/w_0^2(1+i\tau)\approx(1-i\tau)/w_0^2\tau^2$, and defining the parameters below

$$s = x'/w_0\tau,\ s' = z'/w_0\tau,\ \beta = \rho/\delta_0 \tag{5.17}$$

one can obtain such a relationship

$$[x-\rho(l-y')]^2/w_0^2(1+i\tau) \approx s^2(1-i\tau) - 2i\beta\tau' \tag{5.18}$$

If we define the following parameters

$$\begin{aligned} \sigma = \frac{1}{2}b\Delta k,\ \sigma' = \sigma + 4\beta s,\ \xi = l/b \\ \mu = (l-2f)/l, \kappa = \frac{1}{2}\alpha b \end{aligned} \tag{5.19}$$

the SHG intensity $(n_2c/8\pi)|E_2|^2$ will be

$$S(s,s') = 4\pi K(P_1^2k_1^2/\tau^2)\exp[-\alpha' l + \mu\alpha l - 4(s^2+s'^2)]|H(\sigma',\kappa,\xi,\mu)|^2 M^2(x')C^2(x') \tag{5.20}$$

where

$$\begin{aligned} K &= (128\pi^2\omega_1^2/c^2n_1^2n_2)d_{33}^2,\ \alpha' = \alpha_1 + \frac{1}{2}\alpha_2 \\ H(\sigma',\kappa,\xi,\mu) &= (2\pi)^{-1}\int_{-\xi(1-\mu)}^{\xi(1+\mu)} \frac{d\tau'}{1+i\tau'}\exp(-\kappa\tau' + i\sigma'\tau') \end{aligned} \tag{5.21}$$

Apparently, $M^2(x') = 1$. The second harmonic power is then

$$\begin{aligned} P_2 &= \delta_0^2\tau^2(b/2)^2\int\int dsds'S(s,s') \\ &= KP_1^2lk_1\exp(-\alpha' l)h'(\sigma,\beta,\kappa,\xi,\mu) \end{aligned} \tag{5.22}$$

where

$$h'(\sigma,\beta,\kappa,\xi,\mu) = (\pi^2/\xi)\exp(\mu\alpha l)F'(\sigma,\beta,\kappa,\xi,\mu) \tag{5.23}$$

and

$$F'(\sigma,\beta,\kappa,\xi,\mu) = (2/\pi^{1/2})\int_{\infty}^{\infty} ds|H(\sigma+4\beta s,\kappa,\xi,\mu)|^2\exp(-4s^2)C^2(w_0\tau) \tag{5.24}$$

F' can be expressed as

$$F' = F(\sigma,\beta,\kappa,\xi,\mu)G \tag{5.25}$$

where G comes from the spatial modulation of d^2 and

$$\begin{aligned} F(\sigma,\beta,\kappa,\xi,\mu) = (1/4\pi^2)&\int\int_{-\xi(1-\mu)}^{\xi(1+\mu)} d\tau_1'd\tau_2' \\ &\times\frac{\exp[-\kappa(\tau_1'+\tau_2') + i\sigma(\tau_1'-\tau_2') - \beta^2(\tau_1'-\tau_2')^2]}{(1+i\tau_1')(1-i\tau_2')} \end{aligned} \tag{5.26}$$

in which the variables τ_1' and τ_2' are actually both τ', meaning that F is actually an autocorrelation. The factor G is

$$G = \frac{2}{\sqrt{\pi}}\int_{-\infty}^{+\infty}\exp[-(2s - i\beta(\tau_1'-\tau_2'))^2]C^2(w_0\tau s)ds \tag{5.27}$$

There is no double refraction for the fundamental beam in my experiment so the value β is zero. Now we have

$$G = \frac{2}{\sqrt{\pi}}\int_{-\infty}^{+\infty}\exp[-4s^2]C(w_0\tau\cdot s)ds \tag{5.28}$$

where $C(w_0\tau s) = C^2(w_0\tau s)$. Since $s = x'/w_0\tau$,

$$G = \frac{2}{\sqrt{\pi}w_0\tau}\int_{-\infty}^{+\infty}\exp[-\frac{4}{w_0^2\tau^2}x'^2]C(x')dx' = \frac{2}{\sqrt{\pi}w_0\tau}\int_{-\infty}^{+\infty}\exp[-\frac{2}{\tau^2}\frac{2}{w_0^2}x'^2]C(x')dx' \tag{5.29}$$

Under the assumption that the light intensity is constant across a single domain wall, we have the following approximation

$$\frac{2}{\sqrt{\pi}w_0\tau}\int_{-\infty}^{+\infty}\exp[-\frac{2}{w_0^2}x'^2]C(x')dx' \approx \frac{a}{w_0}\frac{2}{\sqrt{\pi}\tau}\int_{-\infty}^{+\infty}\exp[-\frac{2}{w_0^2}x'^2]C'(x')dx' \tag{5.30}$$

where

$$C'(x') = \begin{cases} 1 & x' = m\Lambda/2 + x_0 \\ 0 & otherwise \end{cases} \tag{5.31}$$

in which x_0 is the random position offset, a is the domain wall thickness and $m \in Z$. Besides, as mentioned above,

$$\tau = 2(y - f)/b$$

where $(y - f)$ is the longitudinal distance (along $z-$axis) between the observer (power meter or CCD camera) and the crystal. In my experiments, $\tau \approx 26.1$, as a result,

$$\frac{2}{\tau^2} \approx 0.0029 < 1 \tag{5.32}$$

Thus the approximation Eqn. (5.30) holds for G

$$G \approx \frac{a}{w_0}\frac{2}{\sqrt{\pi}\tau}\int_{-\infty}^{+\infty}\exp[-\frac{2}{\tau^2}\frac{2}{w_0^2}x'^2]C'(x')dx' \tag{5.33}$$

If we assume

$$G' = \frac{2}{\sqrt{\pi}\tau}\int_{-\infty}^{+\infty}\exp[-\frac{2}{\tau^2}\frac{2}{w_0^2}x'^2]C'(x')dx' \tag{5.34}$$

then $G \approx aG'/w_0$. Fig. (5.6) shows the simulation result of the factor G' vs. the domain wall number within the beam waist N for $\tau = 26.1$. The intercept is varying around zero with a very small modulus, and the slope is approximately 0.500. However, if τ is very small, the function $G'(N)$ will not be so linear.

From the numerical simulations, the larger τ is, the more linear $G'(N)$ will be. Usually the coefficient of determination R^2 is used for indicating how well data fit statistical model. The R^2 dependence on τ is shown in Fig. (5.7), from which we can see when $\tau > 0.1$ the function $G'(N)$ will become very linear. In this case, we can say that

$$G \approx aG'/w_0 \approx 0.500aN/w_0 \tag{5.35}$$

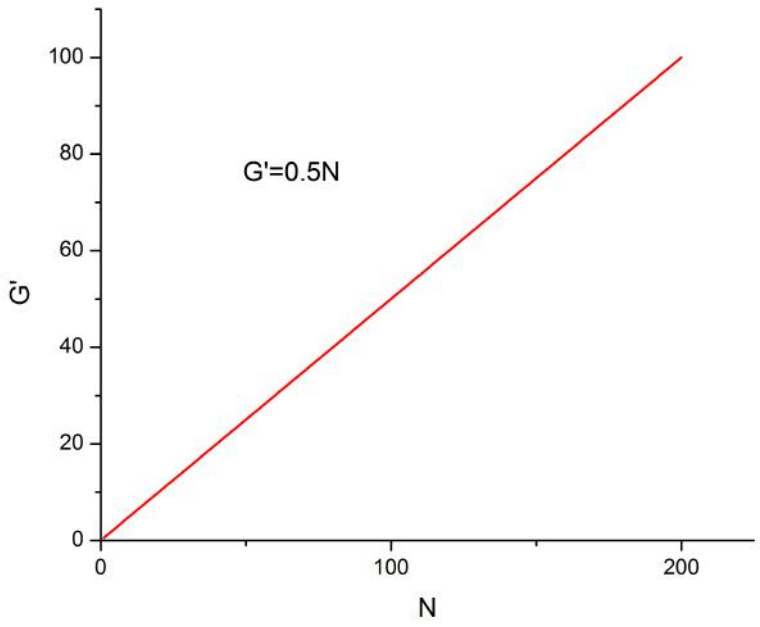

Figure 5.6: The numerical simulation result of G' as a function of domain wall number within the beam waist, in the case of $\tau = 26.1$

If N is substituted with $4w_0/\Lambda$,

$$G \approx 0.500a \cdot 4w_0/\Lambda w_0 = 2a/\Lambda \tag{5.36}$$

So actually the factor $h'(\sigma, \beta, \kappa, \xi, \mu)$ can be expressed as

$$h'(\sigma, \beta, \kappa, \xi, \mu) = h(\sigma, \beta, \kappa, \xi, \mu) \cdot 2a/\Lambda \tag{5.37}$$

where $h(\sigma, \beta, \kappa, \xi, \mu)$ is the h factor in Boyd and Kleinman's notation, which is shown in Fig. (5.8).

Now we can express the Čerenkov SHG power as below

$$P_2 = 2KP_1^2 lk_1 \exp(-\alpha' l)h(\sigma, \beta, \kappa, \xi, \mu)a/\Lambda \tag{5.38}$$

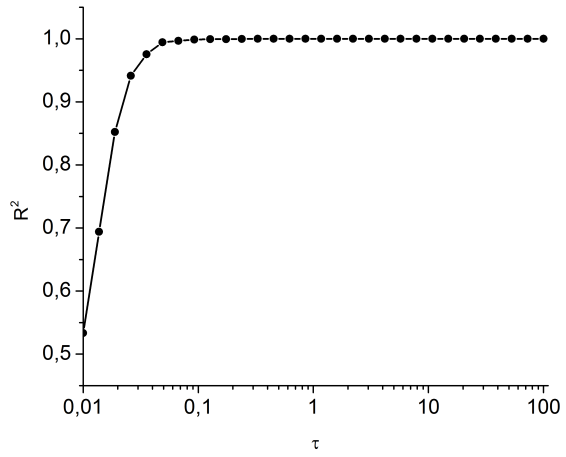

Figure 5.7: The R^2 dependence on τ

5.4 Calibration Curve

In my experiments, different crystals have different grating width l and the pump power varies between different measurement counts, therefore, the CSHG signal power P_2 is normalized in respect to the pump power and the domain grating width

$$P_n = P_2/P_1^2 l \tag{5.39}$$

According to Eqn. (5.38), the normalized power P_n is

$$P_n = 2Kk_1\eta h(0,0,0,\xi,0)a/\Lambda = Kk_1\eta h(0,0,0,\xi,\mu)a \cdot 2/\Lambda \tag{5.40}$$

where P_1, P_2, l, k_1, η, a and Λ are the pump power, the CSHG power, the domain wall grating width, the fundamental wave number, the filter transmission for CSHG, the domain wall thickness and the domain grating period (so $2/\Lambda$ is the domain wall density λ_{dw}) with

$$K = \frac{128\pi^2\omega_1^2 d^2}{c^2 n_1^2 n_2}$$

In order to obtain the CSHG power dependence on the domain density, the CSHG power of periodically poled crystals with four known periods Λ were chosen: 3.18 μm (RKTP), 5.58 μm (KTP) 6.337 μm (RKTP) and 9.01 μm (KTP).

First, in order to test the validity of my experiment principle derived above and the sensitivity of my setup, I did one manual 2D scan across the $b-$facet of each reference crystal with the CCD camera so that the effectiveness of this method could be examined and I could choose uniform regions for the calibration curve.

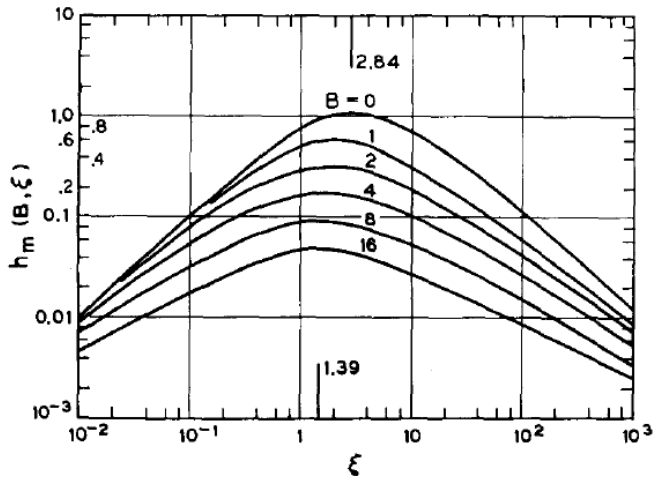

Figure 5.8: $h_m(B, \xi)$ for optimum phase-matching as a function of the focusing parameter $\xi = l/b$ for different values of the double refraction parameter $B = \rho(lk_1)^{1/2}/2$. Reprinted from [53].

The CCD camera response to the light intensity is linear. As a result, I could integrate the brightness of a CSHG spot photograph over all the pixels to get the normalized CSHG power P_n of a certain point in arbitrary unit. I designed the mesh grid on the b-facets, measured the P_n values of the points and converted them into CSHG power maps, where the brightness of the points represents the normalized CSHG power.

The points on the map can be correlated with the images of the polar surfaces, taken by the optical microscope, due to the relatively high resolution of the stage (10 μm). The map for the 3.18 μm reference crystal is shown in Fig. (5.10) (a), and the dark chasm near 4 mm was found to be a large domain merging part shown in Fig. (5.10) (b). At this point, we already see one advantage of CSHG measurements: in-depth information which cannot be obtained from microscopies.

Next, the CSHG powers from the uniform regions of the four reference crystals were measured with the power meter PM2 to obtain the calibration curve. In this step, first I used an optical microscope to identify and choose the regions with correct structures, then I launched the laser beam through them and measured the normalized power. The curve is shown in Fig. (5.9). With it, I can actually evaluate the expected position of the position for sub-μm crystals in ideal cases. In my experiments, the error comes from the power meter PM2 and the domain grating width variation. Therefore the error ΔP_n is then

$$\Delta P_n = P_n\left(\frac{\Delta P_2}{P_2} + \frac{\Delta l}{l} + \frac{\Delta P_1}{P_1}\right) \tag{5.41}$$

In practice, the quantity $\frac{\Delta P_1}{P_1}$ is negligible (about 0.1%). If I would like to use this curve for evaluating the domain wall density of a crystal with unknown structures, from Eqn. (5.39)

$$\frac{\Delta\lambda_{dw}}{\lambda_{dw}} = \frac{\Delta P_2}{P_2} + \frac{\Delta l}{l} \tag{5.42}$$

Consequently,

$$\Delta\Lambda = \frac{2\Delta\lambda_{dw}}{\lambda_{dw}^2} = \Lambda\frac{\Delta\lambda_{dw}}{\lambda_{dw}} \propto \frac{1}{P_2}(\frac{\Delta P_2}{P_2} + \frac{\Delta l}{l}), \quad P_2 \propto \Lambda^{-1} \tag{5.43}$$

So the errors $\Delta\lambda_{dw}/\lambda_{dw}$, $\Delta\Lambda$ and $\Delta\Lambda/\Lambda$ decrease with the domain grating period Λ, meaning the accuracy is higher for sub-μm period crystals.

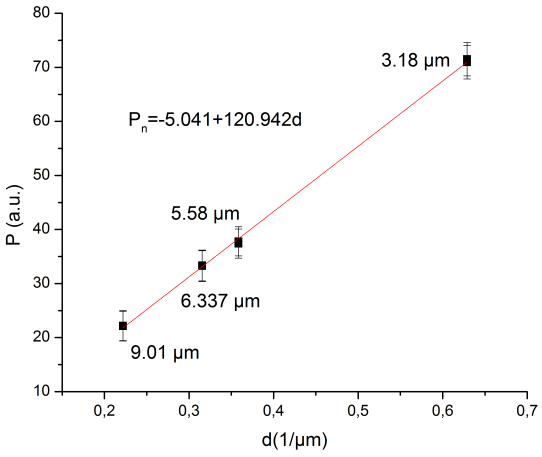

Figure 5.9: The calibration curve obtained from PM2.

5.5 Domain Characterization on Sub-μm Period Crystals

Sub-μm is a tautology for "lower than 1 μm". With the calibration curve obtained, the evaluation of the mean domain wall density in crystals with unknown structures can be conducted. Two crystals with sub-μm structures were evaluated: an RKTP crystal with self-assembled domain gratings and a PPKTP crystal.

With a similar procedure as in the calibration curve step, first I used the optical microscope to identify and choose the regions with good surface and internal condition, namely, the regions where no damage site is present, and then I launched the laser beam in them.

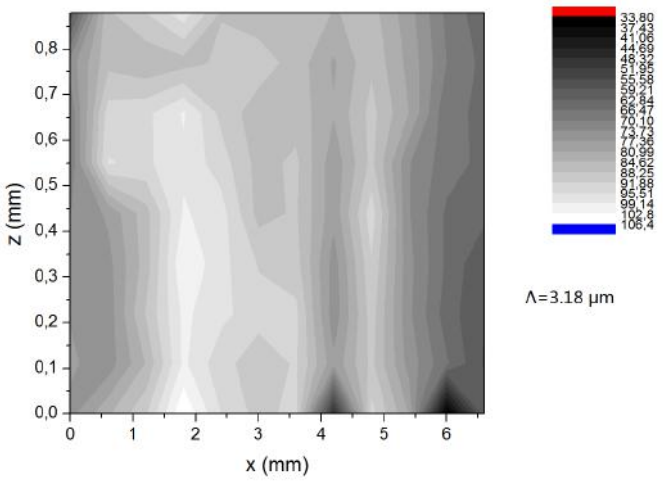

(a)

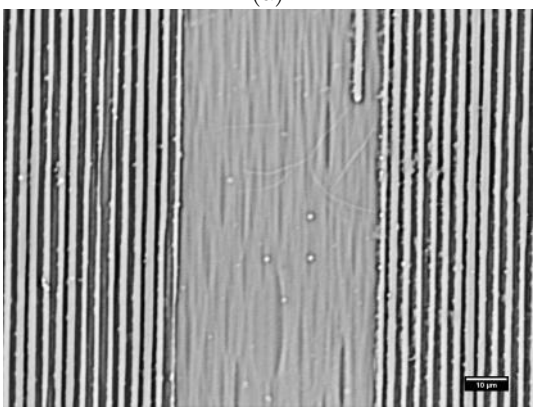

(b)

Figure 5.10: (a) The map of the 3.18 μm reference crystal obtained by the CCD camera. The signal power is in arbitrary unit. (b) The optical microscopic photograph of the 3.18 μm crystal near the dark chasm in (a). The domain missing is clearly visible and it is present on both $c+/c-$ sides.

The first crystal was produced with the self-assembling method [24], so the grating period is relatively random compared to periodically poled crystals. A typical domain structure on the polar $c+$ facet in a self-assembled RKTP crystal is shown in Fig. (5.11 (a)). The SEM photographs of the polar surfaces of the crystal were analyzed with MATLAB, producing the domain wall density (or, the grating period) distribution at the polar surfaces.

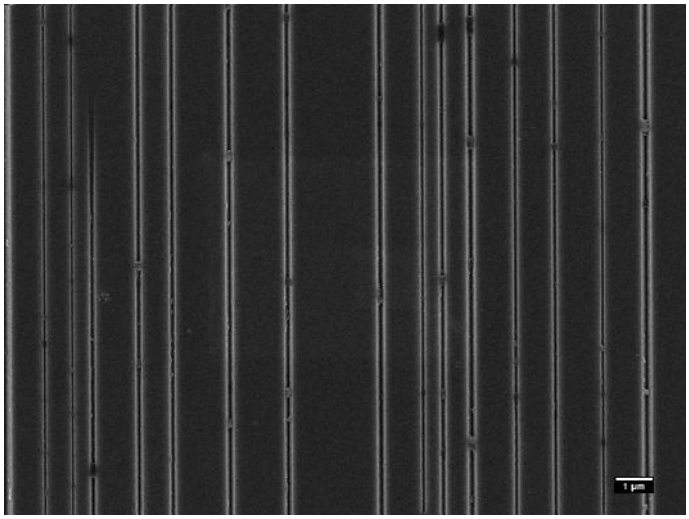

(a)

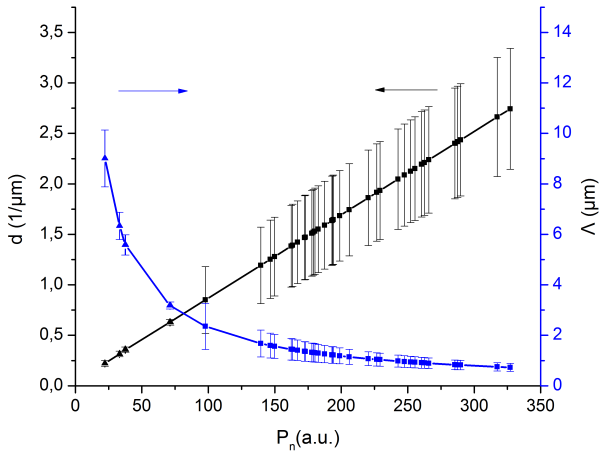

(b)

Figure 5.11: (a) The SEM photograph of the self-assembled sub-µm crystal, c+facet. (b) The domain wall density and the grating period with the errors from the self-assembled and the reference crystals. The triangular and square dots represent the values from reference and self-assembled crystals.

Consequently, I measured the CSHG output of the self-assembled crystal with my experimental setup and converted it into domain wall density using the earlier

obtained calibration curve. The average CSHG power varied between different measurement counts (about 10 nW in PM2). This could be a result of domain wall density variation, surface conditions or misalignment. Besides, the domain grating width l changes along x-direction (around 0.5 mm), introducing an additional error.

The domain wall density as a function of CSHG power is shown in Fig. (5.11 (b)). There was severe damage near the $c-$ facet so I could only measure the region near the $c+$ facet.

The experimental results were compared with the results obtained from SEM photographs and are consistent since the centres of the normal distribution fitting curves for the $c+$ SEM and CSHG distributions are quite close, as shown in Fig. (5.12).

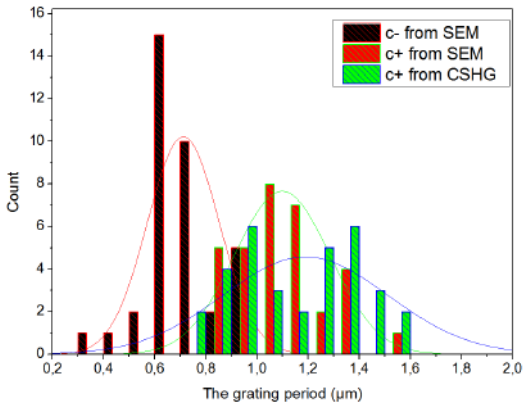

Figure 5.12: The period distribution near the $c+$ facet of the self-assembled crystal. The region near the $c-$ facet had been shot up by a pulse laser previously thus it is not valid to measure with CSHG, for the fundamental beam will be scattered by the damaged parts.

The same principle was used to evaluate the sub-μm PPKTP crystal crystal. The CSHG signal was measured in the region close to both $c+$ and c- facets, and obtained domain density was compared to the one retrieved from SEM photographs of the polar surfaces. The domain grating width variation of this PPKTP crystal is very small, and the readout fluctuation in PM2 was very small as well and can be considered as half the resolution (0.5 nW).

From the chemically etched patterns on the polar surfaces of the crystal, I could only conclude that on $c-$ facet the domain structure is quite ideal with an average grating period of about 700 nm (the desired value) and on $c+$ facet the domain structure is rather random with an average grating period much larger than 700 nm (Fig. (5.13)).

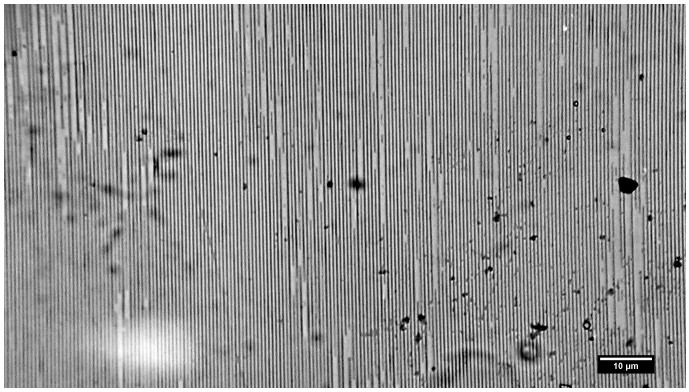

(a)

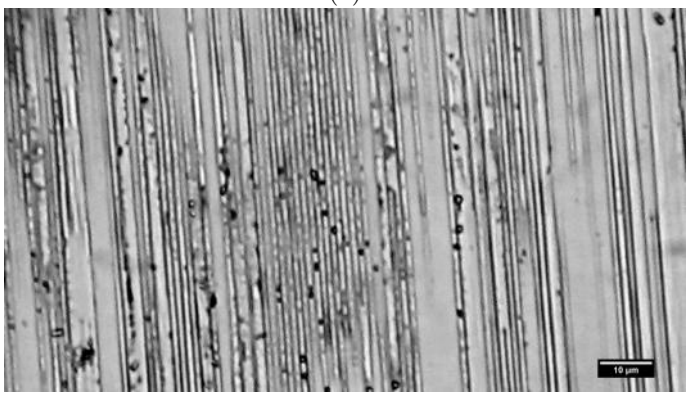

(b)

Figure 5.13: The microscopic photographs of (a) $c-$facet and (b) $c+$facet of the periodically poled sub-μm crystal.

The evaluation of the QPM structure quality along the crystal polar direction and the domain wall density as a function of CSHG power are shown in Fig. (5.14).

From Fig. (5.14 (a)), we can see that the grating periods near c- facet are smaller that those near $c+$ facet, which can be interpreted as the domain merging phenomenon, leading to an increase in the grating period. From Fig. (5.14 (b)), we can see that the grating periods were much lower than expected, from which we can conclude that the poling quality near both polar facets is far from the desired level (a uniform 700 nm grating structure). Although probed just tens of μm below the polar surfaces, it can be concluded that the fine sub-μm structure on the $c-$ facet does not propagate into the bulk i.e. this crystal is only periodic within a very thin layer under the $c-$ facet.

Because only polar facets can be selectively etched, another experiment was

performed on this PPKTP crystal. It was repolished at an angle of $\pi/4$ with the xoz plane and selectively etched as in Fig. (5.15 (a)) and obtained the image shown in Fig. ((5.15 (b)). Again, it shows the fine structure on c- facet does not propagate into the crystal bulk below 60 μm. The pump beam was below the periodic part thus could not probe it.

Once again, it demonstrates the value of this method in evaluating the poling quality in the crystal bulk.

5.6 Nonlinearity Enhancement at Ferroelectric Domain Walls

My theory on CSHG with Gaussian beams is based on such an assumption, that is, in ferroelectric materials, only the ferroelectric domain walls contribute to the CSHG power and the crystal domain bulk do not. So actually after obtaining the calibration curve, the nonlinearity at domain walls can be evaluated.

In practice, the reflection loss cannot be neglected as in the "heuristic" model. For plane waves, we have the Fresnel equations for the s-polarization

$$R_s = \left| \frac{n_1 \cos\theta_i - n_2 \sqrt{1 - \left(\frac{n_1}{n_2}\sin\theta_i\right)^2}}{n_1 \cos\theta_i + n_2 \sqrt{1 - \left(\frac{n_1}{n_2}\sin\theta_i\right)^2}} \right| \tag{5.44}$$

$$T_s = 1 - R_s \tag{5.45}$$

where R_s is the reflectance, n_1, n_2, θ_i are the refractive indices and the incident angle. The propagation of fundamental and CSHG beams in the crystal is shown in Fig. (5.16). Both of them suffer a reflection loss. From Eqn. (4.10), the Čerenkov angle in my experiment satisfies

$$\begin{aligned} \cos\theta_c &= v_2/v_1 = n_1/n_2 \\ \sin\theta_c &= \sqrt{1 - \cos^2\theta_c} \end{aligned} \tag{5.46}$$

According to the Fresnel equations, the transmittance for the fundamental beam at the entrance T_1 and the second harmonics at the exit T_2 are 97.10% and 96.72%, respectively. As a result, Eqn. (5.38) becomes

$$P_2 = 2KP_1^2 l k_1 \eta h(0,0,0,\xi,\mu)(a/\Lambda) \cdot T_1^2 T_2 \tag{5.47}$$

The h factor is 0.4 and the transmission of the filter F2 at 404 nm is 0.8. Applying Eqn. (5.38) the product d^2a in nm and pm/V is calculated to be $2.7173 \times 10^6 (\text{pm/V})^2 \cdot \text{nm}$. The thickness of ferroelectric domain walls is still disputed. According to literature [16][48][54], the range of 10-100 nm may be reasonable. If the domain wall thickness a is 100 nm, the nonlinearity d_{33} at the domain wall is then 164.8 pm/V. Compared to the bulk value 16.9 pm/V [24], it is approximately 9.8

times as large. If we take the value of domain wall thickness as 10 nm, d_{33} at the domain wall becomes 521.3 pm/V, which is 30.8 times as large as the bulk value. However, we do not know the internal structure and the exact definition of ferroelectric domain wall, this is only a conclusion based on my the assumption that only ferroelectric domain walls contribute to CSHG, which needs further verification. If it is true, the reason may be extra broken symmetry at domain walls.

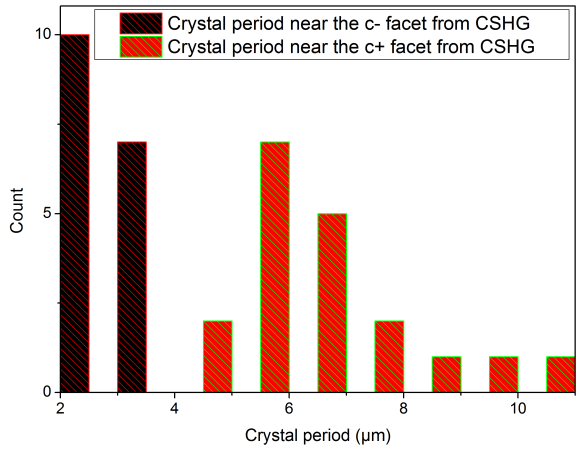

(a)

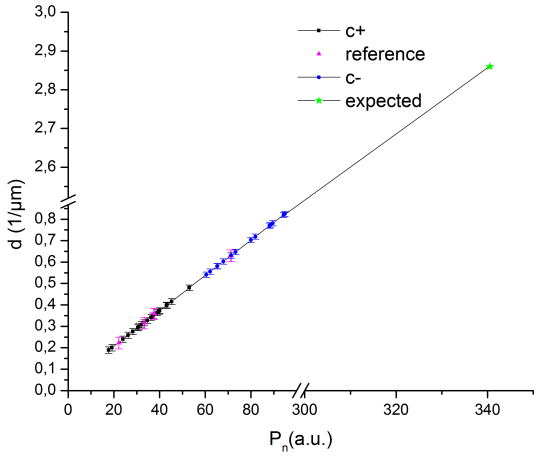

(b)

Figure 5.14: (a) The period distribution near the $c+/c-$ facets of the periodically poled sub-μm crystal. (b) The domain wall density and the grating period with the errors from the periodically poled sub-μm (black square dots for data from near $c+$ facet region and blue round dots for data from near $c-$ facet region) and the reference (magenta triangular dots) crystals. The green pentagram represents the expected position of this crystal, which corresponds to a 700 nm grating period.

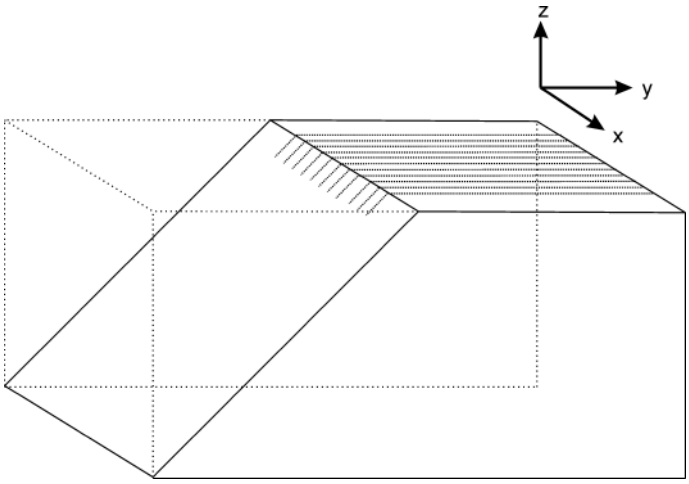

(a)

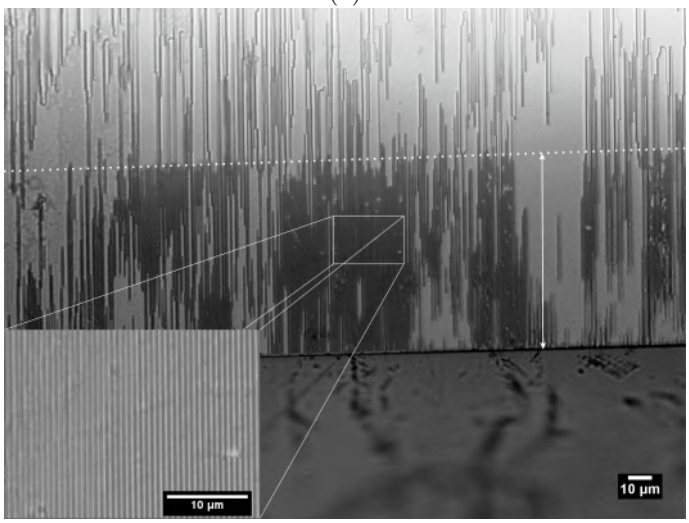

(b)

Figure 5.15: (a) The schematic of the obliquely polished PPKTP crystal. (b) The microscopic photograph of the polar surface for the obliquely polished PPKTP crystal, in which the dashed line and arrow show the periodic region.

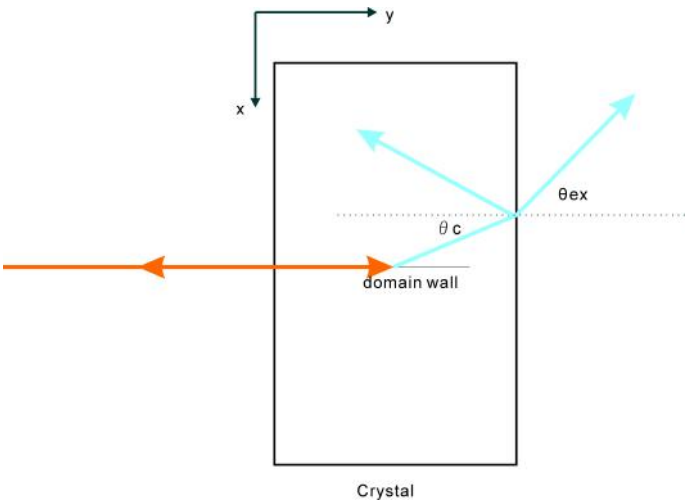

Figure 5.16: The reflections in the experiments.

Chapter 6

Conclusions

As is discussed in Chapter 3, Čerenkov second harmonic generation, in general, can be considered as a consequence of constructive interference. Some current theories on CSHG with Gaussian beams are based on the condition of merely a $\chi^{(2)}$ discontinuity, and the explanation of reciprocal lattice vectors (RLV) is employed. However, this is potentially against the experimental fact that even in a single domain wall ferroelectric crystal CSHG signals can still be detected at the domain walls. Besides, it is probably inconsistent with the experimental fact that the CSHG power increases linearly with the domain grating width, instead of quadratically, as indicated by those theories. By extending Boyd and Kleinman's theory on parametric interaction of focused Gaussian beams in bulk second-order nonlinear materials, I obtained the theory on CSHG of periodically poled QPM crystals without double refraction. According to this, the CSHG power is proportional to the domain wall density, which is twice the reciprocal of the domain grating period.

Furthermore, I established a robust method of evaluating the mean grating period of QPM crystals. By measuring the reference periodically poled QPM crystals and thus obtaining the calibration curve, I can, in theory, convert any normalized CSHG signal power into the period. Due to the decrease of the errors $\Delta\Lambda$ and $\Delta\Lambda/\Lambda$ with the decrease of the domain grating period Λ, this method is highly suitable for sub-μm period crystals. As a result, the goal of a relatively simple and reliable sub-μm domain characterization method is achieved.

From the theoretical and the experimental results described in Chapter 3 and 6, I found that the nonlinearity component d_{33} in (R)KTP could be tens of times as large as the bulk value, depending on the nominal domain wall thickness and the assumption that only domain walls contribute to CSHG power. Thus, the local enhancement in $\chi^{(2)}$ at the ferroelectric domain walls is verified in (R)KTP. However, the cause of this enhancement is still unclear: some argue it is the scattering from the defects near domain walls, others consider it as a local field enhancement (LFE). Based on the literature on ferroic domain walls in thin films, I conclude it is a consequence of a structural broken symmetry at the domain walls, which is

consistent with the necessary condition for the second-order nonlinearity: noncentrosymmetry.

The d-tensor component utilized in this thesis is d_{33}, which means the electric polarizations of both the pump and generated waves are always perpendicular to the xoy plane. In other words, it is a noncritical phase-matching. In the future, the theory of CSHG power with Gaussian beams could be derived for oblique incidence, more nonlinear Čerenkov parametric processes might be studied and other nonlinear coefficients and materials can be tested with such a method, too.

List of Figures

List of Tables

Acknowledgements

First of all, I would like to express my gratitude to my supervisor, Professor Carlota Canalias. Thank you for introducing me into the multicultural Laser Physics Group, where I had a joyful endeavour and gained research experience from this thesis project. It was both exciting and interesting for me to work in darkness and to play with the CSHG light. Furthermore, I learnt a lot in communication skills and scientific methodologies from your precious advice, guide and criticism.

I would also like to thank Professor Valdas Pasiskevicius and Professor Fredrik Laurell. Thank you for teaching me the knowledge of laser physics and nonlinear optics, without which I could never finish the project. I can always get new inspiration and knowledge every time you answer my confusion on optics.

I am very grateful to doctor Andrius Žukauskas. You helped me so many times with your extraordinary experiment expertise and great patience. Thank you very much for sharing me your personal experience for life and research, from which I benefited a lot.

Thank you very much for your generous help, especially your precious KTP crystal, Charlotte Liljestrand.

A special thanks goes to Patrik Holmberg, who helped me a lot in software, from which I learnt how to present information in a professional way.

Thank you for teaching me the knife-edge technique and the great discussions on Austrian economics, Staffan Tjörnhammar.

I would like to express my gratitude to my master program coordinator, Kjell Carlsson. You always answer my questions with a warm smile.

Thank you all, Jens Tellefsen, Michael Fokine, Yen-Chieh Huang, Lars-Gunnar Andersson, Zhangwei Yu, Wenhua Guo, Junsong Peng, Micke Malmström, Nicky Thilmann, Peter Zeil, Gustav Lindgren, Hoda Kianirad and Riaan Coetzee. Whenever I have a problem, you never hesitate to help.

Last, not least, I would like to thank my parents, for they always support me all these years. Without you, I could never realize my dream of studying physics in Sweden.

Bibliography

[1] P. A. Franken, A. E. Hill, C. W. Peters, and G. Weinreich. Generation of optical harmonics. *Phys. Rev. Lett.*, 7:118–119, Aug 1961.

[2] Paul N. Butcher and David Cotter. *The Elements of Nonlinear Optics*. Cambridge University Press, 1990. Cambridge Books Online.

[3] Robert W. Boyd. *Nonlinear Optics, Third Edition*. Academic Press, 3rd edition, 2008.

[4] Amnon Yariv. *Quantum Electronics*. Wiley, third edition, 1989.

[5] Richard L. Sutherland. *Handbook of Nonlinear Optics*. CRC Press, second edition, 2003.

[6] J E Midwinter and J Warner. The effects of phase matching method and of uniaxial crystal symmetry on the polar distribution of second-order non-linear optical polarization. *British Journal of Applied Physics*, 16(8):1135, 1965.

[7] J. A. Armstrong, N. Bloembergen, J. Ducuing, and P. S. Pershan. Interactions between light waves in a nonlinear dielectric. *Phys. Rev.*, 127:1918–1939, Sep 1962.

[8] Amnon Yariv and Pochi Yeh. *Photonics: Optical Electronics in Modern Communications (The Oxford Series in Electrical and Computer Engineering)*. Oxford University Press, Inc., 2006.

[9] Hans Schmid. Some symmetry aspects of ferroics and single phase multiferroics *. *J. Phys.: Condens. Matter*, 20(43):434201, 2008.

[10] Pierre Weiss. L'hypothèse du champ moléculaire et la propriété ferromagnétique. *J. Phys. Theor. Appl.*, 6(1):661–690, 1907.

[11] Bas B Van Aken, Jean-Pierre Rivera, Hans Schmid, and Manfred Fiebig. Observation of ferrotoroidic domains. *Nature*, 449(7163):702–705, 2007.

[12] Jill Guyonnet. Growing up at the nanoscale: studies of ferroelectric domain wall functionalities, roughening, and dynamic properties by atomic force microscopy, doctoral thesis, Jul 2013. ID: unige:31526.

[13] IEEE standard definitions of primary ferroelectric terms. *ANSI/IEEE Std 180-1986*, 1986.

[14] Sergey I Bozhevolnyi, Jørn M Hvam, Kjeld Pedersen, Fredrik Laurell, Hakan Karlsson, Torben Skettrup, and Michele Belmonte. Second-harmonic imaging of ferroelectric domain walls. *Appl. Phys. Lett.*, 73(13):1814–1816, 1998.

[15] Alexander Kirillovich Tagantsev, L Eric Cross, and Jan Fousek. *Domains in ferroic crystals and thin films*. Springer, 2010.

[16] J. Wittborn, C. Canalias, K. V. Rao, R. Clemens, H. Karlsson, and F. Laurell. Nanoscale imaging of domains and domain walls in periodically poled ferroelectrics using atomic force microscopy. *Applied Physics Letters*, 80(9):1622–1624, 2002.

[17] James Patterson and Bernard Bailey. *Solid-State Physics*. Springer Berlin Heidelberg, first edition, aug 2007.

[18] Kwan Chi Kao. *Dielectric Phenomena in Solids*. Academic Press, first edition, mar 2004.

[19] Albert F. Cotton. *Chemical Applications of Group Theory*. Wiley-Interscience, third edition, 1990.

[20] David N. Nikogosyan. *Nonlinear Optical Crystals: A Complete Survey*. Springer, first edition, feb 2005.

[21] Galen D Stucky, Mark LF Phillips, and Thurman E Gier. The potassium titanyl phosphate structure field: a model for new nonlinear optical materials. *Chem. Mater.*, 1(5):492–509, 1989.

[22] F. C Zumsteg, J. D. Bierlein, and T. E. Gier. $K_xRb_{1-x}TiOPO_4$: a new nonlinear optical material. *J. Appl. Phys.*, 47(11):4980–4985, 1976.

[23] I Tordjman, R Masse, and JC Guitel. Structure cristalline du monophosphate $KTiPO_5$. *Zeitschrift für Kristallographie-Crystalline Materials*, 139(1-6):103–115, 1974.

[24] Andrius Žukauskas. *QPM Devices in KTA and RKTP*. Doctoral thesis, Royal Institute of Technology, Jan 2014.

[25] D R Allan, J S Loveday, R J Nelmes, and P A Thomas. A high-pressure structural study of potassium titanyl phosphate (KTP) up to 5 GPa. *J. Phys.: Condens. Matter*, 4(11):2747, 1992.

[26] Yung S. Liu, D. Dentz, and R. Belt. High-average-power intracavity second-harmonic generation using $KTiOPO_4$ in an acousto-optically Q-switched Nd:YAG laser oscillator at 5 kHz. *Opt. Lett.*, 9(3):76–78, Mar 1984.

[27] D.N. Dovchenko, V.A. Dyakov, and V.I. Pryalkin. Growth and applications of potassium titanyl phosphate crystals. *Bull. Acad. Sci. USSR, Phys. Ser.*, 52(2):13–17, 1988.

[28] John D. Bierlein and Herman Vanherzeele. Potassium titanyl phosphate: properties and new applications. *J. Opt. Soc. Am. B*, 6(4):622–633, Apr 1989.

[29] Kecong Zhang and Hong Zhang. Structure-property relationship of potassium titanyl (KTP) isomorphous substituted crystal. *Chinese Science Bulletin*, 43(7):529–536, 1998.

[30] PA Thomas, R Duhlev, and SJ Teat. A comparative structural study of a flux-grown crystal of $K_{0.86}Rb_{0.14}TiOPO_4$ and an ion-exchanged crystal of $K_{0.84}Rb_{0.16}TiOPO_4$. *Acta Crystallographica Section B: Structural Science*, 50(5):538–543, 1994.

[31] P Pernot-Rejmánková, P A Thomas, P Cloetens, T Lyford, and J Baruchel. Structural matching of ferroelectric domains and associated distortion in potassium titanyl phosphate crystals. *J. Phys.: Condens. Matter*, 15(10):1613, 2003.

[32] V.G. Dmitriev and D.N. Nikogosyan. Effective nonlinearity coefficients for three-wave interactions in biaxial crystal of mm2 point group symmetry. *Opt. Commun.*, 95:173 – 182, 1993.

[33] Anton Anema and Theo Rasing. Relative signs of the nonlinear coefficients of potassium titanyl phosphate. *Appl. Opt.*, 36(24):5902–5904, Aug 1997.

[34] Ichiro Shoji, Takashi Kondo, Ayako Kitamoto, Masayuki Shirane, and Ryoichi Ito. Absolute scale of second-order nonlinear-optical coefficients. *J. Opt. Soc. Am. B*, 14(9):2268–2294, Sep 1997.

[35] Göran Hansson, Håkan Karlsson, Shunhua Wang, and Fredrik Laurell. Transmission measurements in KTP and isomorphic compounds. *Appl. Opt.*, 39(27):5058–5069, Sep 2000.

[36] Tso Yee Fan, C. E. Huang, B. Q. Hu, R. C. Eckardt, Y. X. Fan, Robert L. Byer, and R. S. Feigelson. Second harmonic generation and accurate index of refraction measurements in flux-grown $KTiOPO_4$. *Appl. Opt.*, 26(12):2390–2394, jun 1987.

[37] W. Wiechmann, T. Fukui, H. Masuda, and S. Kubota. Refractive-index temperature derivatives of potassium titanylphosphate. *Opt. Lett.*, 18(15):1208–1210, Aug 1993.

[38] G. D. Miller. *Periodically Poled Lithium Niobate: Modeling, Fabrication, and Nonlinear-Optical Performance*. PhD thesis, Stanford University, 1998.

[39] David C. Hanna. Nonlinear frequency conversion in quasi-phase-matching materials. Technical report, ORC, University of Southampton, 2004.

[40] N. Bloembergen and P. S. Pershan. Light waves at the boundary of nonlinear media. *Phys. Rev.*, 128:606–622, Oct 1962.

[41] A. Zembrod, H. Puell, and J.A. Giordmaine. Surface radiation from non-linear optical polarisation. *Opto-electronics*, 1(1):64–66, 1969.

[42] N. Bloembergen, H. J. Simon, and C. H. Lee. Total reflection phenomena in second-harmonic generation of light. *Phys. Rev.*, 181:1261–1271, May 1969.

[43] Anna Fragemann, Valdas Pasiskevicius, and Fredrik Laurell. Second-order nonlinearities in the domain walls of periodically poled $KTiOPO_4$. *Appl. Phys. Lett.*, 85(3):375–377, 2004.

[44] I.V. Shutov, I.A. Ozheredov, A.V. Shumitski, and A.S. Chirkin. Second harmonic generation by femtosecond laser pulses in the laue scheme. *Optics and Spectroscopy*, 105(1):79–84, 2008.

[45] Yan Sheng, Qian Kong, Vito Roppo, Ksawery Kalinowski, Qi Wang, Crina Cojocaru, and Wieslaw Krolikowski. Theoretical study of Čerenkov-type second-harmonic generation in periodically poled ferroelectric crystals. *J. Opt. Soc. Am. B*, 29(3):312–318, 2012.

[46] A. M. Vyunishev, A. S. Aleksandrovsky, A. I. Zaitsev, and V. V. Slabko. Čerenkov nonlinear diffraction of femtosecond pulses. *J. Opt. Soc. Am. B*, 30(7):2014–2021, Jul 2013.

[47] VK Valev, BD Clercq, Xuezhi Zheng, Denitza Denkova, EJ Osley, Stefaan Vandendriessche, AV Silhanek, Vladimir Volskiy, PA Warburton, GAE Vandenbosch, et al. The role of chiral local field enhancements below the resolution limit of second harmonic generation microscopy. 2012.

[48] David A. Scrymgeour and Venkatraman Gopalan. Nanoscale piezoelectric response across a single antiparallel ferroelectric domain wall. *Phys. Rev. B*, 72:024103, Jul 2005.

[49] Alexandr A Kaminskii, H Nishioka, Ken ichi Ueda, W Odajima, M Tateno, K Sasaki, and A V Butashin. Second-harmonic generation with Cherenkov-type phase matching in a bulk nonlinear $LaBGeO_5$ crystal. *Quantum Electronics*, 26(5):381, 1996.

[50] V. Vaičaitis. Cherenkov-type phase matching in bulk KDP crystal. *Optics Communications*, 209:485 – 490, 2002.

[51] Haitao Huang, Deyuan Shen, Jingliang He, Hao Chen, and Yong Wang. Nanosecond nonlinear Čerenkov conical beams generation by intracavity sum frequency mixing in $KTiOAsO_4$ crystal. *Opt. Lett.*, 38(4):576–578, Feb 2013.

[52] Yan Sheng, Andreas Best, Hans-Jürgen Butt, Wieslaw Krolikowski, Ady Arie, and Kaloian Koynov. Three-dimensional ferroelectric domain visualization by Čerenkov-type second harmonic generation. *Opt. Express*, 18(16):16539–16545, Aug 2010.

[53] G. D. Boyd and D. A. Kleinman. Parametric interaction of focused Gaussian light beams. *J. Appl. Phys.*, 39(8):3597–3639, 1968.

[54] Xuewei Deng and Xianfeng Chen. Domain wall characterization in ferroelectrics by using localized nonlinearities. *Opt. Express*, 18(15):15597–15602, Jul 2010.